

Received June 16, 2020, accepted July 4, 2020, date of publication July 8, 2020, date of current version July 21, 2020.

Digital Object Identifier 10.1109/ACCESS.2020.3007877

Development and Demonstration of MIMO-SAR mmWave Imaging Testbeds

MUHAMMET EMIN YANIK^{ID1,2}, (Member, IEEE), DAN WANG¹, (Senior Member, IEEE), AND MURAT TORLAK^{ID2}, (Senior Member, IEEE)

¹Radar and Analytics, Texas Instruments Inc., Dallas, TX 75243, USA

²Department of Electrical and Computer Engineering, The University of Texas at Dallas, Richardson, TX 75080, USA

Corresponding author: Murat Torlak (torlak@utdallas.edu)

This work was supported by the Semiconductor Research Corporation (SRC) through The University of Texas at Dallas' Texas Analog Center of Excellence (TxACE) under Grant 2712.029.

ABSTRACT Multiple-input multiple-output (MIMO) radars and synthetic aperture radar (SAR) techniques are well researched and have been effectively combined for many imaging applications ranging from remote sensing to security. Despite numerous studies that apply MIMO concepts to SAR imaging, the design process of a MIMO-SAR system is non-trivial, especially for millimeter-wave (mmWave) imaging systems. Many issues have to be carefully addressed. Besides, compared with conventional monostatic sampling schemes or MIMO-only solutions, efficient image reconstruction methods for MIMO-SAR topologies are more complicated in short-range applications. To address these issues, we present highly-integrated and reconfigurable MIMO-SAR testbeds, along with examples of three-dimensional (3-D) image reconstruction algorithms optimized for MIMO-SAR configurations. The presented testbeds utilize commercially available wideband mmWave sensors and motorized rail platforms. Several aspects of the MIMO-SAR testbed design process, including MIMO array calibration, electrical/mechanical synchronization, system-level verification, and performance evaluation, are described. We present three versions of MIMO-SAR testbeds with different implementation costs and accuracies to provide alternatives for other researchers who want to implement their testbed framework. Several representative examples in various real-world imaging applications are presented to demonstrate the capabilities of the proposed testbeds and algorithms.

INDEX TERMS Millimeter-wave (mmWave) radar, multiple-input multiple-output (MIMO) radar, synthetic aperture radar (SAR), frequency-modulated continuous-wave (FMCW), back projection algorithm (BPA), range migration algorithm (RMA), three-dimensional (3-D) imaging, testbed design, calibration.

I. INTRODUCTION

The electromagnetic radio waves, which lie within the frequency range of 30 – 300 GHz, are typically known as millimeter-waves (mmWaves) since they correspond to the wavelengths from 10 mm to 1 mm. The mmWaves can penetrate a wide range of optically-opaque and dielectric materials, such as various composites, ceramics, plastic, concrete, wood, and clothing. The radars that operate at mmWave frequencies are very effective in a variety of applications, including medical diagnostics [1]–[5], security screening [6]–[13], non-destructive testing (NDT) of the structures [14]–[16], and aerial imaging [17]–[19]. Besides, mmWave frequencies are non-ionizing and not considered

The associate editor coordinating the review of this manuscript and approving it for publication was Wei Feng ^{ID}.

to be sources of hazardous radiation similar to the signals emitted from walk-through metal detectors (WTMD) [20].

MmWaves can be effectively used for radar imaging systems, which primarily measure the reflectivity of the person/objects in the scene. Comparing with the optical counterparts, mmWave imaging systems require much larger apertures (20 – 200 cm) [16], [21]. Although recent progress in complementary metal-oxide semiconductor (CMOS) technology integrates cost-effective mmWave wideband radar sensors [22], the need for a massive number of sensors to completely build up a high-resolution image of the scene is still a major challenge for mmWave imaging systems. A well-known approach to reduce the hardware complexity while satisfying the data acquisition time requirements in many applications is the realization of a hybrid concept based on the combination of multiple-input multiple-output (MIMO) array

topologies [23]–[25] and synthetic aperture radar (SAR) techniques [26], [27].

Unfortunately, many of the new techniques in this research field are verified using seemingly expensive and custom-built experimental prototypes [7], [28]. Pacific Northwest National Laboratory (PNNL) is one of the pioneers in this area. They produced many interesting results with details on both system architecture and imaging algorithms. Their efforts include imaging instruments with various capabilities [6], [13], [29]. Along with the similar systems reported in [16], [30], these solutions are based on an array of switchable antennas, where the transmitters and receivers are sequentially operated in pairs to be approximated as a monostatic array. Other testbeds such as [31]–[33] utilize a single transmitter and receiver antenna installed on two independent horizontal tracks to achieve an equivalent linear MIMO array with a one-dimensional (1-D) scanning regime. Although these testbeds have the flexibility to emulate different MIMO-SAR configurations, they are highly customized and cannot be easily replicated by others. Besides, they cannot be used to investigate the channel variations in MIMO arrays for calibration, which is an essential topic in practical MIMO-SAR systems.

We believe that many researchers can benefit from low-cost and easy-to-replicate testbeds to validate and demonstrate their MIMO-SAR imaging algorithms. The design process of a MIMO-SAR testbed must consider a wide variety of factors that will determine the quality of reconstructed images. These include calibration, synchronization between the mechanical scans and radar transmissions, motion stability, lateral/range resolution, and accurate aperture sampling. The main contribution of this paper is to provide a complete design guide to build system-level MIMO-SAR mmWave imaging testbeds for a variety of applications and to present comprehensive discussions on important signal processing and hardware/software implementation aspects of a MIMO-SAR testbed framework, which, to the best of our knowledge, have not been studied in the previous literature.

In this paper, we combine commercially available MIMO mmWave radar sensors and different mechanical scanners to facilitate various SAR techniques. We present a novel synchronization mechanism between the scanners and MIMO mmWave sensors to ensure an accurate radar transmission scheme in SAR motion. Many researchers can utilize the introduced novel technique to solve this challenging synchronization problem in their MIMO-SAR testbeds, especially at higher scanning speeds. We propose a practical multi-channel array calibration method to compensate for the gain and phase mismatches of the MIMO array elements. To control the entire signal processing chain of the proposed testbeds, we introduce a custom-developed open-source software toolbox [34], which includes all the testbed control, data capture, calibration, and imaging modules. We present several experimental results from real-world scenarios to demonstrate the effectiveness of our designs that achieve high-resolution

imaging performance in various applications. In fact, with the help of these testbeds, we are able not only to verify imaging algorithms but also to investigate common issues and limitations concerning practical applications. It is important to note that the interested researchers can replace the MIMO mmWave radar sensors discussed in our paper with the terahertz-based counterparts [35]. Hence, they can still benefit from the features of the proposed testbed framework for MIMO-SAR imaging in the terahertz band.

In the presented MIMO-SAR imaging modality, which is implemented by scanning a MIMO mmWave sensor over a planar aperture, both amplitude and phase of the received signal over a wide bandwidth are recorded (coherent data) to mathematically reconstruct focused two-dimensional (2-D) or three-dimensional (3-D) (holographic) images. Thus, employing computationally efficient image reconstruction algorithms is another major challenge of building MIMO-SAR imaging systems, especially in near-field (i.e., short-range) applications. In the near-field, the plane-wave assumption is invalid, and the spherical electromagnetic wave model has to be used. The standard image reconstruction techniques using monostatic sampling schemes, where the measurements are taken by collocated transmit and receive antennas over regular spatial intervals, cannot be directly applied to the proposed MIMO-SAR configurations. The main reason is that one has to take into account the different trajectories of the incident and reflected electric fields for transceiver pairs due to increased separation among them compared with the typical target ranges. As a result, the image reconstruction techniques based on multistatic imaging modalities are necessary for the large MIMO apertures with spatially diverse transmit and receive antennas in SAR configuration. In response to this major challenging requirement, we present and experimentally verify a series of state-of-the-art 3-D image reconstruction algorithms along with the mathematical derivations and demonstrate how to apply these algorithms to the testbed data.

Although the back projection algorithm (BPA) [7], [30], [36], [37] can provide a straightforward solution for arbitrary multistatic array configurations, it suffers from the high computational load in high throughput applications utilizing large MIMO-SAR apertures and wideband sensors. In this paper, the proposed approach in [38] is augmented to improve the performance of the BPA in the SAR axis by solving the problem in the corresponding Fourier domain. The range migration algorithm (RMA) using Fourier-based inversion methods is the most efficient and widely used approach in conventional monostatic SAR imaging for both planar [6], [39] and cylindrical/spherical [29], [40] scanning geometries. In order to extend the RMA to MIMO-SAR configurations, we adopt a multistatic-to-monostatic conversion approach proposed in [41], [42] to transform the multistatic array topology into a monostatic format according to the equivalent phase center principle based on a reference point on the target. On the other hand, the multistatic-to-monostatic conversion technique used in the RMA is precise only for the selected

reference point. Therefore, the fast implementation of more precise wavenumber domain algorithms for the multistatic sampling schemes is necessary for larger target scenes. In this paper, a novel imaging method for single-input multiple-output (SIMO) arrays [31], [43] is adapted to the proposed MIMO-SAR configuration. This method avoids the approximations used in the RMA to improve the image quality as well as reduce the complexity compared with the enhanced BPA.

The rest of the paper is organized as follows. Section II reviews the signal model of the backscattered data and presents the proposed MIMO-SAR configuration. Section III introduces the imaging testbeds built to measure real MIMO-SAR data. Section IV presents the novel radar-scanner synchronization approach implemented to enable higher accuracy in real-time measurements. Section V details the comprehensive open-source software package developed to control the signal processing chain of the testbeds. Section VI proposes a practical calibration method to compensate for the mismatches of the MIMO array elements. Section VII presents different MIMO-SAR image reconstruction algorithms, which exploit the wideband capabilities of mmWave sensors to facilitate 3-D holographic imaging. The imaging results of different real-world application scenarios are reported in Section VIII, which is followed by conclusions.

II. MIMO-SAR SYSTEM MODEL

In this section, we review the wave propagation model of the backscattered MIMO-SAR data, which forms the basis of the image reconstruction problem, present the geometrical setup for the proposed MIMO-SAR system, and introduce the mmWave sensor modules utilized in the testbeds.

A. FMCW CHIRP SIGNAL

We develop our system model based on the mmWave radar sensors that use frequency-modulated continuous-wave (FMCW) chirp signals. The basic principles of FMCW radars are well reported in literature. Here, the behavior of the signal model is reviewed to recall the terminology used throughout the paper. Consider an FMCW signal, the instantaneous frequency of which is expressed as a linear function of time, transmitted by a single transmitter located at (x_T, y_T, Z_0) as

$$m(t) = \cos(2\pi(f_0t + 0.5Kt^2)), \quad 0 \leq t \leq T, \quad (1)$$

where f_0 is the carrier frequency at time $t = 0$, $K = B/T$ is the slope of frequency computed from the sweep bandwidth of B , and the chirp duration of T .

Assuming a single scatterer at (x, y, z) with a complex reflectivity of p , the backscattered signal picked up the receiver element at (x_R, y_R, Z_0) in the delayed and scaled version of the transmitted signal is given as

$$\hat{m}(t) = \sigma m(t - \tau) = \sigma \cos(2\pi(f_0(t - \tau) + 0.5K(t - \tau)^2)), \quad (2)$$

where τ is the round-trip delay of the echo and σ is the combination of target reflectivity and the round-trip amplitude

decay off the target [44], [45]. We define the distances from the transmitter and receiver elements to the point scatterer as

$$\begin{aligned} R_T &= \sqrt{(x - x_T)^2 + (y - y_T)^2 + (z - Z_0)^2}, \\ R_R &= \sqrt{(x - x_R)^2 + (y - y_R)^2 + (z - Z_0)^2}, \end{aligned} \quad (3)$$

respectively, to compute $\sigma = p/(R_T R_R)$ and $\tau = (R_T + R_R)/c$, where c is the speed of light.

The radar then demodulates the received signal by mixing it with the in-phase (I) and quadrature (Q) components of the transmitted signal. This is known as dechirping, which results in a complex beat (or intermediate frequency) signal

$$s(t) = s_I(t) - js_Q(t) = \sigma e^{-j2\pi(f_0t + K\tau t - 0.5K\tau^2)}. \quad (4)$$

Here, the conjugate of the actual FMCW waveform [46] is used as the backscattered data model for the sake of simplicity in the image reconstruction algorithms. The last term of (4) is known as the residual video phase (RVP), which is usually negligible [47], [48]. Therefore, the received beat signal can be expressed in the wavenumber domain as

$$s(x_T, x_R, y_T, y_R, k) = p \frac{e^{-jkR_T}}{R_T} \frac{e^{-jkR_R}}{R_R}, \quad (5)$$

where $k = 2\pi f/c$ is the wavenumber corresponding to the instantaneous frequency $f = f_0 + Kt$.

B. MIMO-SAR CONFIGURATION

Practical MIMO-SAR systems typically combine an array of transceivers with mechanical scanning for high-resolution imaging. In most common MIMO-SAR configurations [32], [49]–[51], a planar aperture is synthesized by mechanically moving a linear MIMO array continuously along a horizontal track pattern, as shown in Fig. 1. In the established right-handed (x, y, z) Cartesian coordinate system, the x -axis represents the horizontal scanning dimension. The y -axis and z -axis denote the vertical and depth directions, respectively. In this system configuration, both the transmitter and receiver arrays are assumed to be linear along the y -axis with a fixed offset of Δ_T along the x -axis.

In the MIMO-SAR sampling scheme that we consider in this paper, an antenna in the transmitting array transmits at wavelength k and every antenna in the receive array simultaneously records the backscattered response. This process is repeated for each transmitting antenna via time-division multiplexing (TDM). The resulting five-dimensional (5-D) data is recorded in $s(x_T, x_R, y_T, y_R, k)$. It is important to note that several types of orthogonal waveforms have been proposed in the literature to be utilized for simultaneous transmission via multiple channels in the context of MIMO-SAR imaging [52].

If each element in the receiver array is assumed to be placed at $x_R = x' - \Delta_T/2$ in the horizontal axis, the horizontal position of each transmitter element is then given as $x_T = x' + \Delta_T/2$. Therefore, the 5-D backscattered data in (5) becomes a four-dimensional (4-D) function

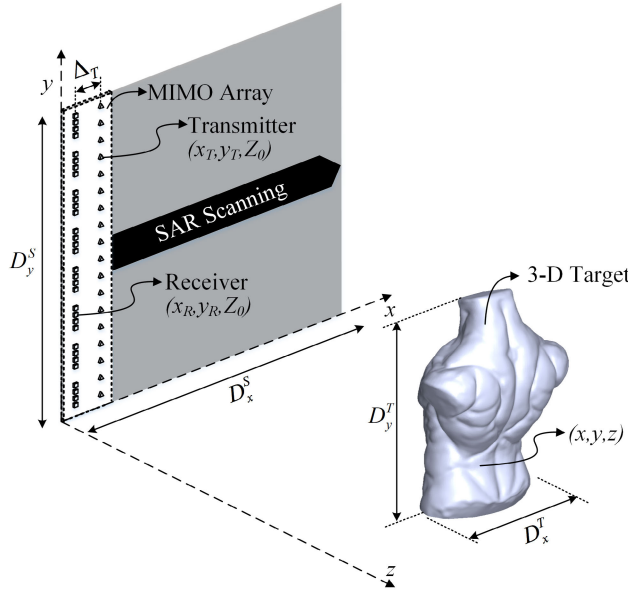


FIGURE 1. The geometry of the MIMO-SAR imaging configuration, where a planar aperture is synthesized by mechanically moving a linear MIMO array.

such that $s(x', y_T, y_R, k)$. Assuming a 3-D target with a reflectivity function $p(x, y, z)$ is located in the scene, we can express the 4-D received backscattered data using (5) and the linearized scattering model after ignoring the amplitude decay with range (i.e., path loss), which is found to be negligible in the short-range applications [6], [39], as

$$s(x', y_T, y_R, k) = \iiint p(x, y, z) e^{-jkR_T} e^{-jkR_R} dx dy dz, \quad (6)$$

where the distances from the transmitters and receivers to the target point in (3) becomes

$$R_T = \sqrt{(x - (x' + \Delta_T/2))^2 + (y - y_T)^2 + (z - Z_0)^2}, \\ R_R = \sqrt{(x - (x' - \Delta_T/2))^2 + (y - y_R)^2 + (z - Z_0)^2}, \quad (7)$$

respectively. The main purpose of the image reconstruction problem, which will be detailed in Section VII, is to recover the complex reflectivity function $p(x, y, z)$ of the 3-D target from the 4-D received data $s(x', y_T, y_R, k)$ captured by each transceiver pair over the xy domain.

C. MIMO mmWave SENSORS

Due to the proliferation of system-on-chip mmWave sensing technology, many commercial off-the-shelf (COTS) radar modules are now available on the market. In this paper, we choose to utilize the modules developed by Texas Instruments. The mmWave sensors used in our testbeds consist of two or three transmit and four receive antenna elements with FMCW transceivers [53]. The transceivers can support up to 4 GHz bandwidth on the 60 – 64 GHz or 77 – 81 GHz frequency band.

Fig. 2a illustrates a typical antenna layout of the evaluation modules based on a single-chip MIMO mmWave sensor with

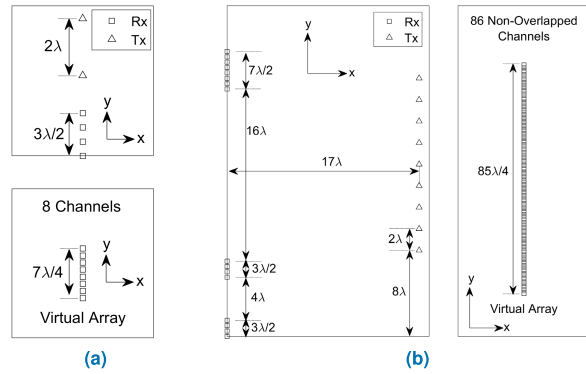


FIGURE 2. The commercially available single-chip radar sensors typically consist of several physically separated transmit and receive antennas. They can be mapped to a virtual array for fast data processing. The virtual arrays consist of co-located transmit and receive antenna elements. For example, (a) a single-chip mmWave sensor with two transmit and four receive antennas can be mapped to a virtual array with eight elements. (b) It is also possible to cascade multiple chips to increase the aperture size. A four-chip cascaded mmWave radar module with nine transmit and 16 receive antennas can create a virtual array of 86 non-overlapped elements.

two transmitters and four receivers. In this layout, the receive antennas are uniformly spaced along y -axis by $\lambda/2$ (tuned to the center frequency). The transmit antennas are also located along y -axis with 2λ spacing. The horizontal offset between the linear transmit and receive arrays is $\Delta_T = 0$. The evaluation modules that enable three transmitters have a similar layout with the exception of their third transmit antenna, which is in the middle of the transmit array in y -axis and has an offset of $\lambda/2$ along x -axis [53]. To create a linear MIMO array as shown in Fig. 1, the third transmit antenna in the three-transmitter versions is switched-off, and only two transmit antennas, which share the same position with the receive array along the axis of motion (i.e., x -axis), are used. In other words, a linear virtual array consists of eight elements, which are uniformly spaced along y -axis by $\lambda/4$, is created as shown in Fig. 2a.

As illustrated in Fig. 2a, a single-chip MIMO mmWave sensor consists of a handful of transmitter and receivers. As a result, multiple sensor chips must be cascaded to create moderately large array apertures [54]. In this paper, an available MIMO radar module from Texas Instruments, which is a combination of four single-chip mmWave sensors [55], is used. Each sensor has four receive and three transmit antennas. As illustrated in the physical antenna layout in Fig. 2b, the receive antennas from each chip are grouped and uniformly spaced in y -axis by $\lambda/2$. The transmit antennas from three chips are uniformly spaced along y -axis by 2λ . The remaining three transmit antennas from one of the chips, which are not shown in Fig. 2b, have offsets along x -axis. Therefore, these transmit antennas are switched-off to create a linear MIMO array and only the nine uniformly distributed transmit antennas are used along with all 16 receive antenna elements. The horizontal offset between the linear transmit and receive arrays is $\Delta_T = 17\lambda$. With this configuration, a virtual array of 86 non-overlapped channels along y -axis

is achieved, where the virtual elements are uniformly distributed with an inter-element spacing of $\lambda/4$, as shown in Fig. 2b.

D. REALIZATION OF THE MIMO-SAR CONFIGURATION

The MIMO-SAR configuration presented in Section II-B utilizes an $N_T \times N_R$ element linear MIMO array, where N_T and N_R are the numbers of transmit and receive antennas, respectively, in SAR configuration to discretely sample the continuous MIMO-SAR aperture plane. In this configuration, the total number of transmitting and receiving elements arranged over the vertical axis is assumed to be sufficient to create a large MIMO aperture (D_y^S) required for high-resolution while satisfying the Nyquist criterion to avoid aliasing. However, as summarized in Section II-C, most commercially available MIMO mmWave sensors typically have few transmit and receive antennas. Hence, the effective aperture sizes of both single-chip and four-chip cascaded sensors are not enough to achieve high cross-range resolution along the y -axis [44], [56].

In this paper, we propose to synthesize a 2-D aperture by mechanically moving the MIMO mmWave sensors continuously across the xy plane, along a parallel track pattern, as depicted in Fig. 3. The MIMO-SAR aperture is uniformly sampled in x spatial domain with a sampling distance of Δ_x . Using the virtual channel concept [24], [57], [58] and selecting the sampling distance in y -axis as $\Delta_y = M\lambda/4$, where $M = 8$ and $M = 86$ for the single-chip and four-chip cascaded sensors, respectively, the MIMO-SAR aperture is assumed to be uniformly sampled in y spatial domain also. The total effective aperture sizes in both axes are then approximated by $D_x \approx (N_x - 1)\Delta_x$ and $D_y \approx N_y(M - 1)\lambda/4$, where

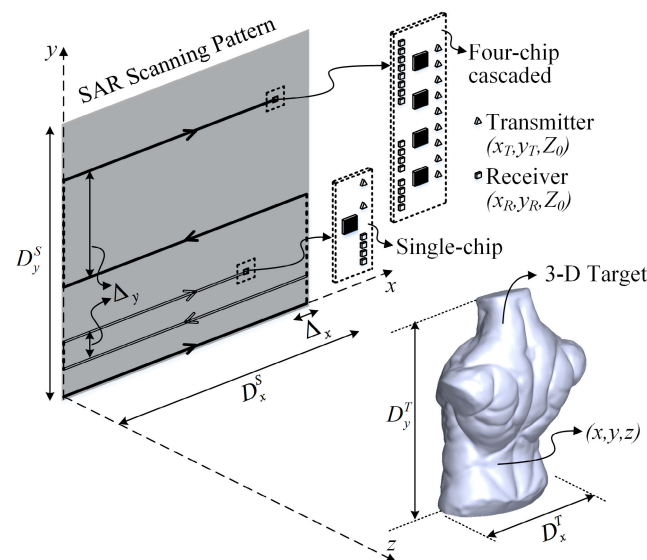


FIGURE 3. A 3-D target is scanned by a single-chip or a four-chip cascaded MIMO mmWave sensor following a rectangular pattern. The spacing between horizontal scans (Δ_y) depends on the size of the MIMO array.

N_x is the total number of measurement points along x -axis, and N_y is the total number of horizontal scans along y -axis.

In this paper, we develop a highly reconfigurable testbed framework to combine commercially available MIMO mmWave sensors with motorized xy scanners by utilizing the industry standard communication interfaces in embedded systems. The researchers can benefit from the proposed testbeds to demonstrate various MIMO-SAR configurations by integrating their own front-end boards with different MIMO antenna layouts or performing a particular scanning trajectory.

III. IMAGING TESTBEDS

In this section, we present different types of MIMO-SAR imaging testbeds that we built throughout this research. Our prototypes uniquely combine system-on-chip MIMO mmWave sensors and SAR signal processing techniques. To synthesize a large aperture over the target scene, different versions of mechanical scanners with two-axis motorized rail systems are designed and implemented. Both single-chip and multi-chip cascaded wideband mmWave sensors are integrated with the scanners to generate high-resolution 3-D holographic images of the target scene. Based on the COTS mmWave evaluation modules and stepper motors based rail systems, the presented testbeds are low-cost and highly reconfigurable.

In our previous studies, two different MIMO-SAR imaging testbeds are presented briefly using both single-chip [11], [56], [59] and multi-chip cascaded [60] mmWave sensors to validate the proposed image reconstruction algorithms and to investigate different performance metrics. In this paper, our goal is to focus on the system-level design perspective in more detail. Besides, we present an enhanced version of the testbed and mention the improvements implemented in the previous versions. The system architectures and the basic features of each prototype are described in detail, and their suitability for future research purposes are illustrated.

A. VERSION I

In this section, the first version of the MIMO-SAR mmWave imaging testbeds prototyped in [11], [56], [59] is summarized to provide a complete study and to demonstrate the improvements presented in this paper. The testbed shown in Fig. 4a consists of four major components: (1) a single-chip mmWave sensor, (2) a low-cost two-axis mechanical scanner, (3) a motion controller, and (4) a host personal computer (PC).

The mmWave sensor is a combination of three hardware modules from Texas Instruments: (1) IWR1443-Boost, (2) mmWave-Devpak, and (3) TSW1400 boards [53]. The IWR1443-Boost is an evaluation module based on the single-chip IWR1443 mmWave sensor, which integrates four receive and three transmit antennas, as discussed in Section II-C. The TSW1400 and mmWave-Devpak are add-on boards used with Texas Instrument's mmWave

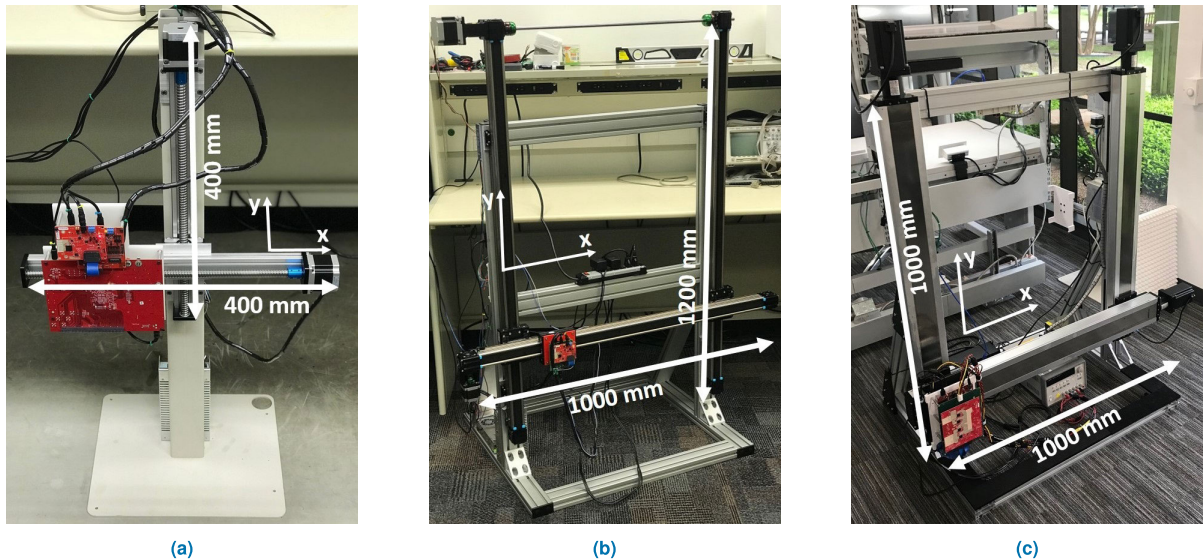


FIGURE 4. Imaging testbeds: (a) Version I: single-chip mmWave sensor based imaging testbed with limited speed and aperture size. (b) Version II: single-chip mmWave sensor based imaging testbed utilizing a faster scanner with larger aperture size. (c) Version III: four-chip cascaded mmWave sensor based imaging testbed.

sensors to enable high-speed raw analog-to-digital converter (ADC) data capture. The TSW1400 module captures the data from the IWR1443-Boost module through the mmWave-Devpak and stores the formatted data into its onboard memory. Captured raw data are then imported to the host PC with a serial port for post-processing.

The other component of the imaging testbed is the two-axis mechanical scanner built using two ball screw linear rails and stepper motors. The scanner provides movements in horizontal and vertical directions. The radar hardware stack is installed on the horizontal track by which an equivalent 2-D scanning is achieved. The maximum scanning ranges in both horizontal and vertical directions are 400 mm. The motor controller, which is configured to operate linear rails at a maximum speed of 20 mm/s, is connected to the host PC with a serial port. Compared with the testbed presented in our previous study, AMC4030 motion controller [61], which is a low-cost general-purpose COTS product, is used to establish a common framework for all the testbed versions.

While the first prototype has limited dimensions and scanning speed, our goal was to demonstrate the proof-of-concept. The details of the enhanced imaging systems with bigger dimensions and much faster scanning speeds are introduced in the following sections.

B. VERSION II

In this section, an enhanced version of the single-chip mmWave sensor based imaging testbed utilizing a bigger and faster custom-built two-axis mechanical scanner is presented. This testbed is designed for high-speed scanning of a larger SAR aperture to enable more flexibility in solving different signal processing problems and investigating various performance metrics. In the following, the system architecture and the proposed enhancements are described in detail.

The testbed shown in Fig. 4b consists of four major components: (1) a single-chip mmWave sensor, (2) an improved two-axis mechanical scanner, (3) a motion controller, and (4) a host PC, similar to the version I. In addition, a novel radar-scanner synchronization module, which will be detailed in Section IV, is implemented to enable higher accuracy in the data capture process. The diagram shown in Fig. 5 is a simplified view of the main elements and the high-level system architecture of the imaging testbed.

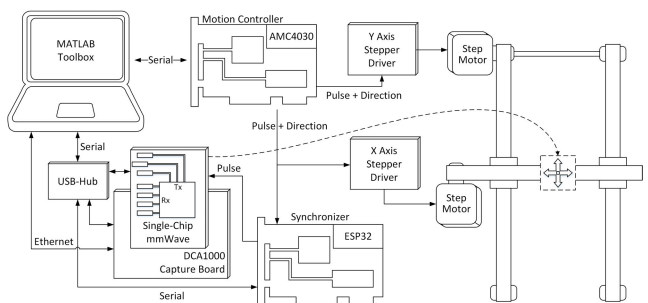


FIGURE 5. The high-level system architecture of the version II testbed consists of a single-chip mmWave sensor and a bigger and faster mechanical scanner.

The new testbed utilizes the mmWave sensor consisting of IWR1443-Boost, mmWave-Devpak, and TSW1400 modules, similar to the version I. Besides, it is also configured to be interfaced with the DCA1000 evaluation module, which is a real-time data capture board for interfacing with Texas Instrument's mmWave sensors [53]. The DCA1000 module captures the raw ADC data from the IWR1443-Boost module and streams the packetized data to the host PC over Ethernet.

Compared with the version I, an enhanced solution suitable for faster scanning operations at a maximum speed of 500 mm/s is developed using a 1 meter by 1.2 meters

automatic rail system. An effective way to increase the speed is to change from a ball screw to a belt mechanism. Therefore, in the new version, belt-driven linear rails [62] are used. To improve the stability, two coupled rails are used along the vertical direction, as depicted in Fig. 4b and Fig. 5.

The enhanced version of testbed presented in this section is capable of supporting our future research, such as investigating the Doppler effect in faster speeds, integration of multiple mmWave sensors for distributed MIMO analysis, etc.

C. VERSION III

As discussed in Section II-D, compared with the single-chip based solutions, utilizing the multi-chip cascaded sensors in MIMO-SAR testbeds reduces the total data acquisition time to fulfill the demand of various real-world applications. In this section, we detail our novel combination of the multi-chip cascaded MIMO mmWave sensors and SAR, whose initial version is briefly summarized in [60].

The testbed shown in Fig. 4c consists of five major components: (1) a four-chip cascaded mmWave sensor, (2) a two-axis mechanical scanner, (3) a motion controller, (4) a synchronization module, and (5) a host PC. The diagram shown in Fig. 6 is a simplified view of the main elements and the high-level system architecture of the imaging testbed.

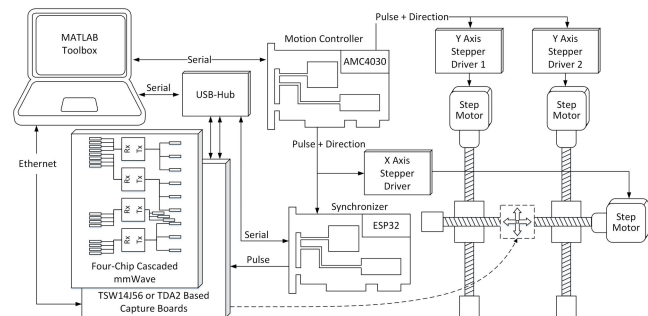


FIGURE 6. The high-level system architecture of the version III testbed consists of a four-chip cascaded mmWave sensor.

The mmWave sensor is a combination of the four-chip cascaded front-end board, which is introduced in Section II-C, and TSW14J56 based add-on interface modules from Texas Instruments [55] to enable high-speed raw ADC data capture. The interface boards provide the connectivity between the four-chip cascaded mmWave front-end module and the host PC to acquire the raw ADC data. The data captured from the mmWave sensor are stored into the onboard memory of the TSW14J56 module. Stored data are then imported to the host PC with a serial port for post-processing. Alternatively, the new generation TDA2 processor based evaluation boards [55] can also be used to provide a real-time processing foundation for the four-chip cascaded mmWave front-end modules over Ethernet in MIMO-SAR imaging.

In the version III testbed, a 1 meter by 1 meter two-axis mechanical scanner is built using three identical linear rails. Compared with the previous testbeds, the faster versions of the ball screw linear rails [61] are used along with more

powerful stepper motors to improve the payload capacity while maintaining the high operation speed. With this configuration, a maximum speed of 400 mm/s in both axes is achieved. As illustrated in Fig. 4c and Fig. 6, the horizontal rail is mounted on two vertical rails, which are operated by separate stepper motors and drivers. The stepper drivers dedicated to the vertical rails are connected to the same port of the motion controller to ensure a coupled scanning along the vertical direction.

IV. SYNCHRONIZATION BETWEEN THE SCANNER AND RADAR

The standard way of synchronizing the scanner and mmWave radar sensor assumes constant speed at the scanner during the entire horizontal motion and uniform radar transmissions in the time domain. By considering an initial synchronization between the scanner and mmWave sensor, a uniform radar sampling in the spatial domain is assumed to be achieved. In the testbed version I, which is presented in Section III-A, this approach is adopted. The motion start and the radar trigger commands (i.e., the software trigger feature of the sensors) are sent separately via the MATLAB-based toolbox (will be detailed in Section V) for each horizontal scan. The inter-chirp sampling time of the mmWave sensor is then configured based on the speed of the platform to achieve the desired sampling distance in the spatial domain.

At higher speeds, to start and stop the stepper motors in a smooth way without stalling, control of the acceleration and deceleration is needed. Hence, the constant speed assumption is invalid, and an alternative technique must be developed. In this paper, a novel solution for the scanner-radar synchronization is designed and implemented in the testbeds version II and III, which are presented in Section III-B and Section III-C, respectively. The proposed solution accurately synchronizes the scanner with radar independent of the speed and acceleration profiles.

In all the testbeds developed in this paper, the motion controllers generate pulse signals at variable rates to move both stepper motor based ball screw and belt-driven linear rails at desired speeds. This control scheme requires no other sensors for positioning and makes the overall design an open-loop system. The position and speed of the rails are controlled precisely just by sending pulses from the motion controller to the stepper drivers, as illustrated in Fig. 5 and Fig. 6.

In the proposed synchronization solution, a pulse counter module is implemented on an ESP32-based microcontroller [63] running freeRTOS [64]. This module counts the number of pulses generated by the motion controller for the horizontal scan. The radar signal transmission is then triggered (using the hardware trigger feature of the sensors) after a threshold event, which is configured by the desired sampling distance Δ_x , occurs in the pulse counter module. The diagram in Fig. 7 illustrates the control sequence of the improved synchronization approach.

Fig. 8a shows the pulse diagrams recorded using the version II testbed detailed in Section III-B. The scanner is

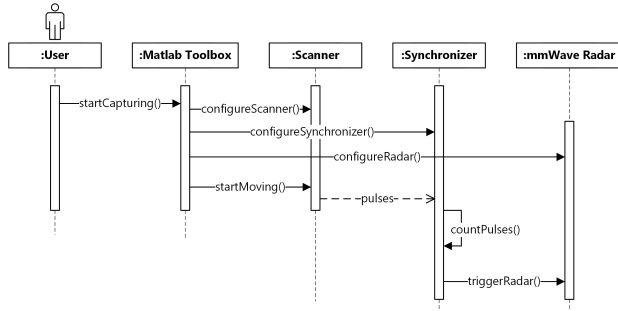


FIGURE 7. The proposed synchronization approach between the scanner and mmWave radar, which accurately synchronizes the testbed independent of the speed and acceleration profile.

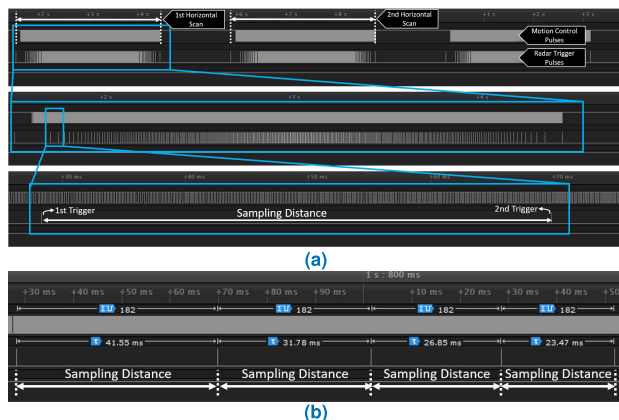


FIGURE 8. (a) The pulse diagram of the enhanced synchronization approach for an example scenario: $D_x^s \approx 400$ mm, $\Delta_x \approx 1$ mm, and the maximum speed is 500 mm/s. (b) Close-up of the pulse diagram to show four consecutive radar triggers in detail. The inter-sampling time is non-uniform because of the acceleration profile.

configured to move $D_x^s \approx 400$ mm along each horizontal scan at a maximum speed of 500 mm/s. The synchronization module is configured such that a sampling distance of $\Delta_x \approx 1$ mm is realized. The belt-driven linear rail utilized in the version II testbed moves 110 mm per 20000 pulses according to its design specifications. Therefore, the synchronization module triggers the radar when a pulse threshold event (i.e., 182 pulses) occurs in the pulse counter module to ensure a uniform sampling in the spatial domain. The detailed pulse diagram in Fig. 8b, which includes four consecutive radar triggers, illustrates the accuracy in the proposed synchronization mechanism and the non-uniform inter-sampling time caused by the acceleration profile. It is shown that the radar trigger instants based on the accurate pulse threshold events (i.e., 182 pulses) ensure a uniform sampling in the spatial domain.

V. IMAGING TOOLBOX

In this section, we develop a comprehensive open-source MIMO-SAR imaging toolbox [34], which is a MATLAB [65] based software package including the complete signal processing chain of the prototyped solutions.

The toolbox allows the user to control the testbeds and to reconstruct high-resolution 3-D holographic images using the captured experimental data. We develop the toolbox in MATLAB platform since it is widely used in the scientific and technical world.

The developed toolbox consists of three main modules: (1) data capture, (2) MIMO array calibration, and (3) image reconstruction, as illustrated in the flow diagram in Fig. 9. The mathematical framework of the MIMO array calibration and image reconstruction modules are detailed in Section VI and Section VII, respectively. This section summarizes the data capture module, which is implemented in a graphical user interface (GUI) based application.

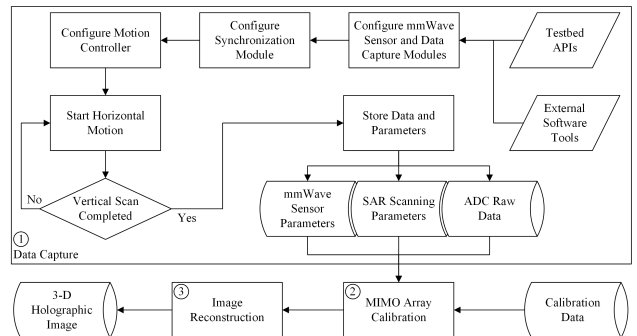


FIGURE 9. The high-level data flow diagram of the imaging toolbox.

In the data capture mode, each hardware module of the testbed (introduced in Section III) is controlled through dedicated application programming interfaces (APIs). While the toolbox communicates directly with the motion controller and synchronization modules, it needs to be integrated with two additional software applications to communicate with the mmWave sensor and data capture modules. The mmWave Studio application [53] provides a set of API commands to communicate with the Texas Instruments' mmWave sensors over the serial interfaces of the host PC. The DCA and TDA2 modules are also controlled through the mmWave Studio for raw ADC data capture over Ethernet. Similarly, the APIs provided by the High Speed Data Converter (HSDC) Pro application [53] are used to configure the TSW data capture modules and to import the raw ADC data to the host PC for post processing.

The user configures the mmWave sensor parameters and generates the desired SAR scenario via three different menu tabs of the GUI as shown in Fig. 10. The menu tab shown in Fig. 10a is used to initialize the communication interfaces of the testbed modules and to configure the scanner and mmWave sensor parameters. The desired SAR parameters are configured via the scenario generation menu tabs shown in Fig. 10b and Fig. 10c, which are developed based on the basic and enhanced synchronization approaches (detailed in Section IV), respectively. The toolbox then handles the fully-automated data capture process according to the realized MIMO-SAR configuration (discussed in Section II-D), as demonstrated in Fig. 9.

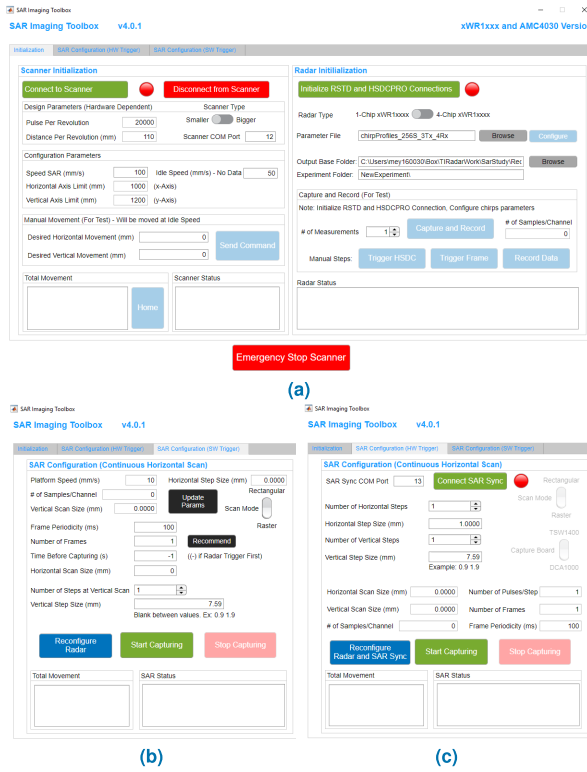


FIGURE 10. MATLAB GUI for MIMO-SAR imaging. (a) Platform and radar configuration menu tab. SAR scenario generation menu tabs based on (b) basic and (c) enhanced synchronization approaches.

VI. MIMO ARRAY CALIBRATION

In a practical system, measurement errors in the MIMO array may arise due to sensor gain and phase mismatches [66], [67]. These mismatches can be caused by various reasons, such as path length imperfections, chip-to-chip or antenna-to-antenna variations, etc. Especially, phase mismatches can affect the image reconstruction adversely, and lead to unacceptable defocused blur and range shift in the images. Therefore, calibration is an essential step in MIMO-SAR imaging to reduce the effects of channel variations and to improve the reconstructed image quality.

Different calibration procedures have been studied in the previous literature [68]–[72]. In this paper, we utilize the testbeds we developed to propose a practical calibration method based on the ideal backscattered signal model from a reference point target (i.e., a corner reflector) at an unknown position. The accuracy of the proposed approach depends on the reference beat signal, which needs a precisely positioned point target. Therefore, the first step in the calibrating process is to estimate the unknown (x, y, z) position of the reference target accurately. To achieve that, as depicted in Fig. 11a, we first propose to capture data along both horizontal and vertical axes using a single transceiver antenna pair of the MIMO array, which is assumed to be a single monostatic virtual element, as a reference channel.

As detailed in Section II-A, the total round-trip delay of the backscattered data is directly related to the frequency

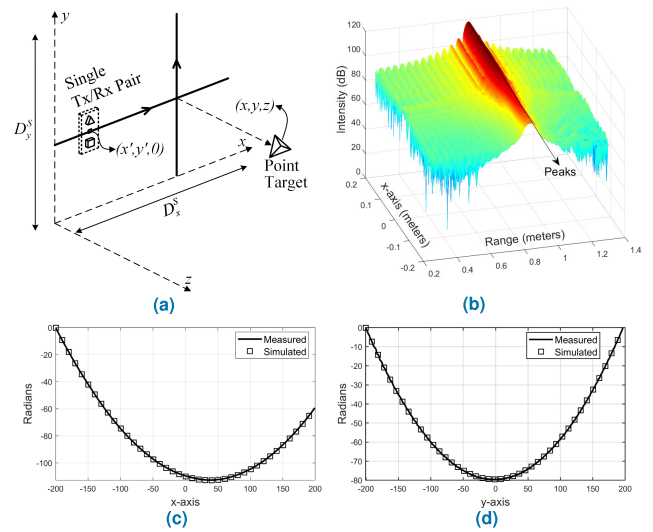


FIGURE 11. (a) The data capture configuration using a single channel to estimate the position of the reference target. (b) The range FFT output of the single channel data along the x -axis. The unwrapped phase of the range FFT complex peak gains measured along the (c) x -axis and (d) y -axis.

and phase of the measured beat signal in (4). Defining the captured wideband beat signal $s(x', y', t)$ as a 3-D function of time t and measurement points over the xy domain, the goal is to estimate an accurate range profile of the target using the beat frequency and phase at each measurement point.

Let us define the backscattered 3-D beat signal from an ideal point target using the signal model in (4) after ignoring the amplitude and RVP terms as

$$s(x', y', t) \approx e^{j(2\pi f_b(x', y')t + \phi(x', y'))}, \quad (8)$$

where $f_b(x', y') = K\tau(x', y')$ and $\phi(x', y') = 2\pi f_0 \tau(x', y')$ are the frequency and phase of the beat signal, respectively, which are both functions of the round-trip delay

$$\tau(x', y') = 2\sqrt{(x - x')^2 + (y - y')^2 + z^2}/c, \quad (9)$$

at each measurement point. We assume that we have uniformly sampled version of the beat signal over the time domain as $s[x', y', n] = s(x', y', nT_s)$, where T_s is the sampling period and $n = [0, \dots, N - 1]$. Then, we can estimate the frequency and phase in (8) by taking an N -point discrete-time Fourier transform (DTFT) on the sampled beat signal as

$$\begin{aligned} S(x', y', e^{j\omega}) &= \sum_{n=0}^{N-1} e^{j(\omega_b(x', y')nT_s + \phi(x', y'))} e^{-j\omega n} \\ &= e^{j\phi(x', y')} e^{-j[(\omega - \omega_b(x', y')T_s)(N-1)/2]} \\ &\quad \times \frac{\sin[(\omega - \omega_b(x', y')T_s)N/2]}{\sin[(\omega - \omega_b(x', y')T_s)/2]}, \end{aligned} \quad (10)$$

where $\omega_b(x', y') = 2\pi f_b(x', y')$ is the angular beat frequency. Because the beat signal is assumed to be uniformly sampled over time, the sampled version of (10) can be obtained by

performing a fast Fourier transform (FFT) operation, which is usually referred to as the range FFT [48].

In Fig. 11b, the range FFT output of an example scenario at a fixed y location is shown. In this scenario, a corner reflector is located at a distance of 800 mm in front of the scanner. The scanning aperture length along the x -axis is $D_x^S = 400$ mm. As depicted in the range FFT result, the variation of the target range is very small within a single beat signal. Therefore, to obtain a more accurate range profile, which is a function of the round-trip delay in (9), we need to utilize the phase of the beat signal $\phi(x', y')$ in (8).

If we select $\hat{\omega} = \omega_b(x', y')T_s$ in (10) for all measurement points, i.e., the beat frequency corresponding the peak index of the FFT output, the complex values at that index will only have the phase terms $e^{j\phi(x', y')}$. The residual phase error caused by the limited FFT resolution is assumed to be negligible [48]. Using the range FFT output in Fig. 11b, the unwrapped phase of the range FFT peaks measured over the x -axis is depicted in Fig. 11c along with the simulated version. Similarly, the unwrapped phase of the range FFT peaks measured and simulated along the y -axis is shown in Fig. 11d. This approach can also be used to diagnose problems with the testbed. For example, Fig. 12 shows a similar phase track along the y -axis, which is measured using a mechanically unstable scanner. Hence, such an analysis can help the researchers to diagnose the possible vibration and instability problems of the mechanical parts of their testbeds.

The position (x, y, z) of the point target referenced to the scanning geometry can be estimated by applying the least squares curve fitting approaches [73] to the measured beat signal phase. These approaches directly result in an estimate of the target position by finding the set of parameters, which minimizes the squared error between the modeled and measured phase as

$$\{\hat{x}, \hat{y}, \hat{z}\} = \arg \max_{x, y, z} \sum_{\langle x', y' \rangle} |\hat{\phi}(x', y') - 2\pi f_0 \tau(x', y')|^2, \quad (11)$$

where $\tau(x', y')$ is a function of the target location (x, y, z) as given in (9). Here, we assume that the actual distance between the radar aperture and the point target shown in Fig. 11a is available in the measured beat signal phase. However, in a practical setting with FMCW signaling scheme, a range FFT operation can be used to provide the estimate of the target range as $\hat{R}(x', y') = R(x', y') + R_b$, where $R(x', y') = c\tau(x', y')/2$ is the actual target distance from the known measurement point (x', y') and R_b is the range bias imposed by the hardware imperfections. Hence, the last step in the position estimation problem is to compensate for the range bias R_b of the reference channel. In this paper, we propose to exploit the coupling between the transmitting and receiving antenna elements [68], [74] to estimate the range bias.

The target-independent range bias resulting from the mutual coupling can be obtained by observing the range profile of the beat signal as shown in Fig. 13a. Let us assume that the reference channel consists of the u th transmitter and

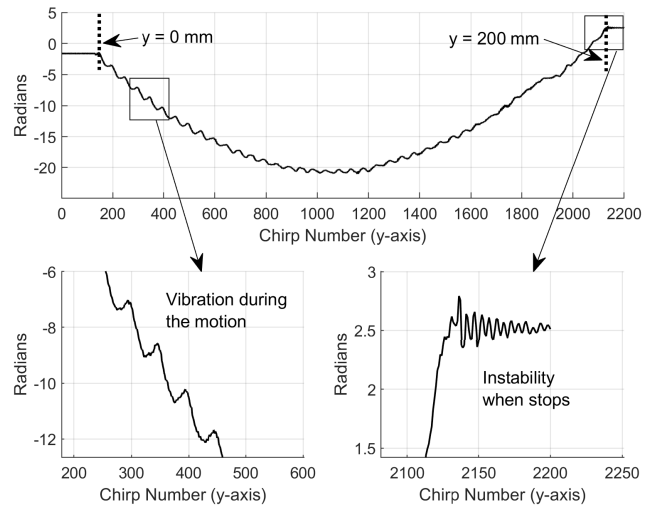


FIGURE 12. The unwrapped phase of the range FFT complex peak gains measured along the y -axis when the scanner is mechanically unstable.

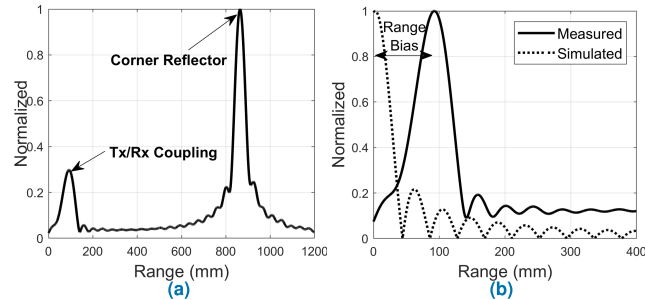


FIGURE 13. The range FFT of the measured beat signal: (a) including the measured mutual coupling and the corner reflector data, (b) including the measured and simulated mutual coupling data.

v th receiver elements located at $\mathbf{r}_u \in \mathbb{R}^3$ and $\mathbf{r}_v \in \mathbb{R}^3$, respectively. Then the range bias can be estimated from the reference beat signal modeled using the Euclidean distance between the corresponding transceiver antenna pair $|\mathbf{r}_u - \mathbf{r}_v|$, as illustrated in Fig. 13b.

Now, we are ready to create the reference backscattered signal model for each channel of the MIMO array based on the estimated target location (x, y, z) to be used in the calibration process. Let us define the total round-trip delay $\tilde{\tau}_\ell$ of the FMCW signal reflected off the point target between the u th transmit and v th receive antennas, and the corresponding transceiver gain a_ℓ . We model the delays between antenna pairs as the superposition of a common instrument delay and residual delays between antenna elements: $\tilde{\tau}_\ell = \tau_i + \tau_\ell$. Ignoring the additive noise and RVP term, the uncalibrated measured beat signal can be defined as

$$\tilde{s}_\ell(t) = a_\ell e^{j2\pi(f_0+Kt)(\tau_i+\tau_\ell)} = \underbrace{a_\ell e^{j\psi_i}}_{\eta_\ell} \underbrace{e^{j2\pi f_i t}}_{w_\ell(t)} s_\ell(t), \quad (12)$$

where $s_\ell(t)$ is the reference beat signal model, $f_i = K\tau_i$ is the beat frequency that cause a range bias in the system as

mentioned before, and η_ℓ is the residual complex gain factor. Given the measurements $\tilde{s}_\ell(t)$, the calibration error signal can be computed by a simple demodulation process

$$w_\ell(t) = \tilde{s}_\ell(t)s_\ell^*(t) \approx \eta_\ell e^{j2\pi f_i t}, \quad (13)$$

where $(.)^*$ denotes the complex-conjugate operation. Estimating f_i and η_ℓ from (13) reduces to the parameter estimation problem of a single-frequency complex tone from noisy observations [75], [76]

$$\hat{f}_i = \arg \max_f \sum_{\ell} |W_\ell(f)|^2, \quad (14)$$

where $W_\ell(f)$ is defined as

$$W_\ell(f) = \int_0^T w_\ell(t)e^{-j2\pi ft} dt. \quad (15)$$

If the data $w_\ell(t)$ is uniformly sampled in t , the FFT can be used to obtain the discrete version of $W_\ell(f)$. Fig. 14a and Fig. 14b show the FFT output $W_\ell(f)$ of the calibration signals $w_\ell(t)$ for each channel of the single-chip and multi-chip cascaded mmWave sensors, respectively.

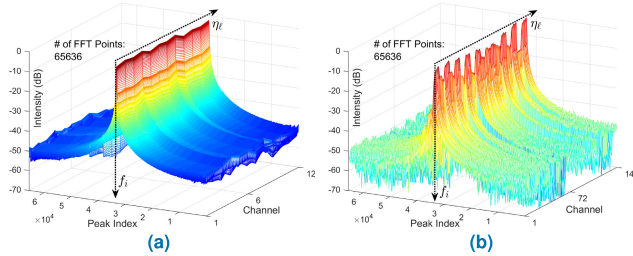


FIGURE 14. The FFT output of the calibration signals for each channel of the: (a) single-chip and (b) multi-chip cascaded mmWave sensors.

Finally, the complex gain factors η_ℓ for each transceiver pair can be computed by plugging the estimate \hat{f}_i in (12). Fig. 15a and Fig. 15b show the estimated phase of the complex gain factor and the range bias for each channel of the single-chip mmWave module, respectively. Similarly, the estimated phase of the complex gain factor and the range bias for each channel of the four-chip cascaded mmWave module (only for the 144 channels created by the uniformly located transmitter antennas, as detailed in Section II-D) are illustrated in Fig. 15c, and Fig. 15d, respectively.

VII. EXAMPLES OF 3-D IMAGE RECONSTRUCTION ALGORITHMS WITH MIMO-SAR

In this section, we present examples of efficient 3-D image reconstruction algorithms suitable for the proposed MIMO-SAR configuration. The presented algorithms are compared in both precision and computational complexity. It is important to emphasize that having access to the testbed framework proposed in this paper allows researchers not only to verify but also to develop new algorithms [77] as well as refine the techniques presented in the following sections.

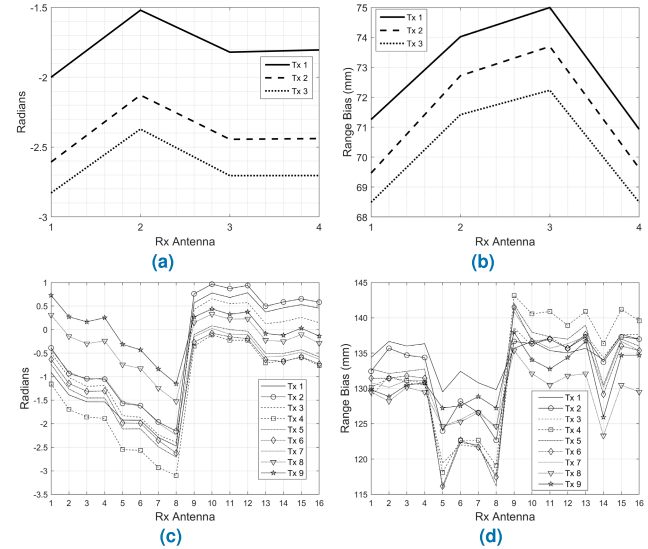


FIGURE 15. The calibration parameters of the single-chip and multi-chip cascaded mmWave sensors: (a) the phase of the complex gain factor, and (b) the range bias of the 12 channels of the single-chip sensor. (c) the phase of the complex gain factor, and (c) the range bias of the 144 channels of the multi-chip cascaded sensor.

A. ENHANCED BACK PROJECTION ALGORITHM

In this section, we augment the proposed method in [38] according to the terminology and system configuration used throughout this paper. In this study, the complete wideband MIMO array is modeled as a combination of multiple single-tone single-input single-output (SISO) multistatic structures.

Using the well-known BPA [7], [36], [38], (6) can be reformulated to recover the reflectivity function $p(x, y, z)$ from the received backscattered data $s(x', y_T, y_R, k)$ as

$$p(x, y, z) = \iiint s(x', y_T, y_R, k) e^{jkR_T} e^{jkR_R} dx' dy_T dy_R dk. \quad (16)$$

Taking (7) into (16) and defining

$$h(x, y, z, y_T, y_R, k) = e^{jk\sqrt{(x-(\Delta T/2))^2 + (y-y_T)^2 + (z-z_0)^2}} \times e^{jk\sqrt{(x+(\Delta T/2))^2 + (y-y_R)^2 + (z-z_0)^2}}, \quad (17)$$

which is the matched filter computed for all transceiver pairs, wavelengths, and target points, the reconstruction problem can be represented as

$$p(x, y, z) = \iiint s(x', y_T, y_R, k) \times h(x-x', y, z, y_T, y_R, k) dx' dy_T dy_R dk. \quad (18)$$

In (18), the first integral is a convolution relation in the x -domain. Therefore, taking the Fourier transform with respect to x on both sides of (18) yields

$$P(k_x, y, z) = \iiint S(k_x, y_T, y_R, k) \times H(k_x, y, z, y_T, y_R, k) dy_T dy_R dk, \quad (19)$$

where k_x is the corresponding wavenumber coordinate. Since the backscattered data is assumed to be discretely sampled at each wavelength k and each (y_T, y_R) locations, the remaining integrals in (19) are turned into summations on discrete values to calculate $P(k_x, y, z)$, which yield the final 3-D image as

$$p(x, y, z) = \text{IFT}_{1D}^{(k_x)}[P(k_x, y, z)], \quad (20)$$

where $\text{IFT}_{1D}^{(k_x)}$ is the 1-D inverse Fourier transform operation over the k_x -domain.

The presented method here is similar to the golden-standard BPA. It only improves the performance in the x -axis (i.e., the SAR domain) by solving the image reconstruction problem in the corresponding wavenumber-domain (i.e., k_x -domain). This method provides high imaging precision by coherently accumulating the received signal from each transceiver pair at each wavelength, and can be used for arbitrary array configurations. However, its computational complexity, which can be approximated as $O(N^5 \log N)$ [38], is still too high for 3-D MIMO-SAR imaging.

B. RANGE MIGRATION ALGORITHM FOR MIMO-SAR

The RMA is the most efficient and widely used method in conventional monostatic sampling schemes [6], [39]. However, due to multistatic configuration, it cannot be directly applied to MIMO-SAR imaging in short-range operations. To adopt the existing Fourier-based image reconstruction techniques based on monostatic sampling schemes for multistatic imaging systems with large MIMO apertures, a phase compensation approach is needed. Here, in order to extend the RMA for MIMO-SAR, a multistatic-to-monostatic conversion operation according to a reference point in the target space is used.

Let us denote the location of the phase center associated with the transmitter element at $(x' + \Delta_T/2, y_T, Z_0)$ and the receiver element at $(x' - \Delta_T/2, y_R, Z_0)$ as (x', y', Z_0) . Defining a reference point (x_0, y_0, z_0) in the target domain, the received multistatic data set $s(x', y_T, y_R, k)$ can be converted to the effective monostatic version as [41], [42]

$$\tilde{s}(x', y', k) = s(x', y_T, y_R, k) \frac{\hat{s}_0(x', y', k)}{\hat{s}_0(x', y_T, y_R, k)}, \quad (21)$$

where

$$\begin{aligned} \hat{s}_0(x', y_T, y_R, k) &= e^{-jk(\hat{R}_T + \hat{R}_R)}, \\ \hat{s}_0(x', y', k) &= e^{-jk\hat{R}}, \end{aligned} \quad (22)$$

are the backscattered data model for the multistatic and the corresponding monostatic array, respectively, assuming a target domain that contains a single ideal point scatterer at the reference point (x_0, y_0, z_0) . In (22), \hat{R}_T and \hat{R}_R are the distances from the transmit and receive antennas to the reference point, respectively, and \hat{R} is the distance between the corresponding phase center and the reference point. Using the approximation developed in [56], (21) can be further simplified as

$$\tilde{s}(x', y', k) = s(x', y_T, y_R, k) e^{-jk\left(\frac{\Delta_T^2 + d_T^2}{4(z_0 - Z_0)}\right)}, \quad (23)$$

where Δ_T and d_T are the distances between the transmitter and receiver elements along the x and y axes, respectively.

Now we are ready to introduce the RMA to reconstruct the 3-D target image using the multistatic-to-monostatic converted backscattered signal in (21) and (23). Assuming the linearized scattering model with the target reflectivity of $p(x, y, z)$ similar to (6), we can express the effective monostatic version of the backscattered data from a 3-D target as

$$\tilde{s}(x', y', k) = \iiint p(x, y, z) e^{-jkR} dx dy dz, \quad (24)$$

where R is the distance between the phase center of the transceiver elements and the target points in the 3-D space. Substituting the Weyl's idea of the representation of a spherical wave as a superposition of plane waves [78], [79]

$$e^{-jkR} \approx \iint e^{-j(k_x(x-x') + k_y(y-y') + k_z(z-Z_0))} dk_x dk_y, \quad (25)$$

into (24) and using the Fourier transform definitions, the backscattered data spectrum becomes

$$\tilde{S}(k_x, k_y, k) = P(k_x, k_y, k_z) e^{jk_z Z_0}, \quad (26)$$

where the wavenumber components k_x , k_y , and k_z corresponding to x , y , and z , respectively, must satisfy

$$k_z = \sqrt{4k^2 - k_x^2 - k_y^2}, \quad k_x^2 + k_y^2 \leq 4k^2. \quad (27)$$

In (26), the backscattered data spectrum $\tilde{S}(k_x, k_y, k)$ is assumed to be uniformly sampled in k -domain. Hence, resampling the data to uniformly spaced positions in k_z -domain [39], [80] using the dispersion relation in (27), the ultimate 3-D image reconstruction can be carried out as

$$p(x, y, z) = \text{IFT}_{3D}^{(k_x, k_y, k_z)}[e^{-jk_z Z_0} \tilde{S}(k_x, k_y, k_z)], \quad (28)$$

where $\tilde{S}(k_x, k_y, k_z)$ is the resampled backscattered data spectrum into the uniform k_z grid and $\text{IFT}_{3D}^{(k_x, k_y, k_z)}$ denotes 3-D inverse Fourier transform operation over the $k_x k_y k_z$ domain.

The presented technique first converts the measurement data from multistatic-to-monostatic, and then performs a holographic image reconstruction by utilizing the existing Fourier-based methods with reduced computational complexity (compared with the enhanced BPA), which can be approximated as $O(N^3 \log N)$ [6], [39].

C. SIMO-SAR BASED IMAGE RECONSTRUCTION

In this section, to solve the entire MIMO-SAR imaging problem, we first decompose the MIMO array into several single-tone SIMO multistatic structures, which are composed of different single transmitting elements and a common receiving array. We then coherently sum all the SIMO-SAR subimage results to form the ultimate reconstruction.

Using the signal model in (6), we can express the received backscattered data of the n th SIMO-SAR configuration as

$$s_n(x', y_R, k) = \iiint p(x, y, z) e^{-jkR_n} e^{-jkR_R} dx dy dz, \quad (29)$$

where

$$s_n(x', y_R, k) = s(x', y_T, y_R, k)|_{y_T=y_n}, \quad (30)$$

is the backscattered data from the n th transmitting antenna located at (x', y_n, Z_0) . In (29), R_n and R_R are the distances from the transmitter and receiver elements of the corresponding SIMO array to the target point, respectively. In this section, the image reconstruction algorithm is derived assuming a 1-D MIMO array, where the horizontal offset between the transmitter and receiver arrays in (7) is $\Delta_T = 0$. Hence, the spherical wave propagation terms both for transmit and receive paths in (29) can be decomposed into the superposition of plane waves as [78], [79]

$$e^{-jkR_n} \approx \int e^{-j(k_x(x-x')+k_z^T\sqrt{(y-y_n)^2+(z-Z_0)^2})} dk_x, \quad (31)$$

$$e^{-jkR_R} \approx \iint e^{-j(k_x(x-x')+k_y^R(y-y_R)+k_z^R(z-Z_0))} dk_x dk_y^R, \quad (32)$$

where k_x and k_y^R , which represent the Fourier transform variables corresponding to x and y_R axes, respectively, must satisfy the following condition

$$-k \leq k_x \leq k, \quad -k \leq k_y^R \leq k, \quad (33)$$

and k_z^T and k_z^R are defined as

$$k_z^T = \sqrt{k^2 - k_x^2}, \quad k_z^R = \sqrt{k^2 - k_x^2 - (k_y^R)^2}. \quad (34)$$

Taking (31) and (32) into (29), and taking the Fourier transform on both sides with respect to x (the distinction between the primed and unprimed coordinate systems are dropped) and y_R yield [31]

$$S_n(2k_x, k_y^R, k) = \iint P(2k_x, y, z) e^{-jk_z^T\sqrt{(y-y_n)^2+(z-Z_0)^2}} \times e^{-jk_y^R y} e^{-jk_z^R(z-Z_0)} dy dz, \quad (35)$$

where $S_n(2k_x, k_y^R, k)$ is the 2-D Fourier transform of $s_n(x, y_R, k)$ with respect to x (in $2k_x$ spectral domain) and y_R , and $P(2k_x, y, z)$ is the 1-D Fourier transform of $p(x, y, z)$ with respect to x (in $2k_x$ spectral domain). In (35), because k_z^T is a function of k_x as given in (34), the right hand side of the equation can not be expressed directly into a Fourier transformation. Here, we augment the proposed method in [31] to solve the SIMO-SAR problem by clarifying the reconstruction steps in more detail using the approach in [43] given for SIMO-only configurations.

First, let us rewrite the relation between the received signal and the target reflectivity in (35) as

$$\tilde{S}_n(2k_x, k_y^R, k) = \iint \tilde{P}_k(2k_x, y, z) e^{-jk_y^R y} e^{-jk_z^R z} dy dz, \quad (36)$$

where

$$\tilde{S}_n(2k_x, k_y^R, k) = S_n(2k_x, k_y^R, k) e^{jk_z^R Z_0}, \quad (37)$$

is the compensated backscattered data using the dispersion relation in (34), and

$$\tilde{P}_k(2k_x, y, z) = P(2k_x, y, z) e^{-jk_z^T\sqrt{(y-y_n)^2+(z-Z_0)^2}}, \quad (38)$$

is the target reflectivity with a phase modulation, which is caused by the spatial offset between the transmitting element and the target point. Equation (36) shows the Fourier transform relation between $\tilde{S}_n(2k_x, k_y^R, k)$ and $\tilde{P}_k(2k_x, y, z)$. However, this relation only holds for a specific wavelength k since the dependency of $\tilde{P}_k(2k_x, y, z)$ on k . Therefore, (36) can be rewritten using the dispersion relation in (34) and the Fourier transform definitions as

$$\begin{aligned} \tilde{P}_{k_i}(2k_x, k_y^R, k_z^R) \\ = \tilde{S}_n(2k_x, k_y^R, k_i) \delta\left(k_i - \sqrt{k_x^2 + (k_y^R)^2 + (k_z^R)^2}\right), \end{aligned} \quad (39)$$

where the subscript k_i indicates that only the measurements corresponding to wavenumber k_i are used, $\tilde{P}_{k_i}(2k_x, k_y^R, k_z^R)$ is the 2-D Fourier transform of $\tilde{P}_k(2k_x, y, z)$ with respect to y and z , and $\delta(\cdot)$ is the impulse function. Evaluating the inverse Fourier transform on both sides of (39) with respect to k_z^R using (34), and then taking the inverse Fourier transform on both sides with respect to k_y^R yield

$$\tilde{P}_{k_i}(2k_x, y, z) = \text{IFT}_{1D}^{(k_y^R)} \left[\tilde{S}_n(2k_x, k_y^R, k_i) e^{j\sqrt{k_i^2 - k_x^2 - (k_y^R)^2} z} \right], \quad (40)$$

where $\text{IFT}_{1D}^{(k_y^R)}$ denotes 1-D inverse Fourier transform operation over the k_y^R -domain. Using (38) and (34), the 3-D reflectivity at the wavelength k_i can be estimated from (40) as

$$p_{k_i}(x, y, z) = \text{IFT}_{1D}^{(2k_x)} \left[\tilde{P}_{k_i}(2k_x, y, z) e^{j\sqrt{k_i^2 - k_x^2} \sqrt{(y-y_n)^2 + (z-Z_0)^2}} \right], \quad (41)$$

where $\text{IFT}_{1D}^{(2k_x)}$ denotes 1-D inverse Fourier transform operation over the $2k_x$ -domain. The result obtained by (41) can be regarded as a subimage produced by the measurements of n th SIMO-SAR configuration at a single wavelength k_i . Therefore, letting k_i go through all the available wavelengths and sum up all the $p_{k_i}(x, y, z)|_{y_T=y_n}$ subimages from each transmitter yield the ultimate 3-D MIMO-SAR image as

$$p(x, y, z) = \sum_n \sum_i p_{k_i}(x, y, z)|_{y_T=y_n}. \quad (42)$$

The presented technique in this section avoids the multistatic-to-monostatic conversion and wavenumber domain interpolation steps in the RMA for MIMO-SAR to achieve a better precision. Compared with the enhanced BPA, it reduces the computational complexity, which can be approximated as $O(N^4 \log N)$. Besides, it needs looser restrictions than the RMA for MIMO-SAR that the transmitters (or receivers according to the reciprocity) can be arbitrarily positioned.

VIII. MEASUREMENTS AND IMAGING RESULTS

Together with the non-ionizing character and the ability to “look-through” most nonmetal materials, the complete imaging solutions proposed in this paper are suitable for several valuable applications. In this section, the presented image

reconstruction algorithms are implemented to the data measured using the prototyped testbeds in different real-world scenarios.

The FMCW chirp configuration is an important step in the image reconstruction process. The commercially available FMCW mmWave sensors detailed in Section II-C provide flexibility in configuring chirp parameters [81]. In all experiments, FMCW waveforms are configured to vary from $f_0 = 77.33$ GHz to 80.91 GHz (the bandwidth $B = 3.58$ GHz), where the signal with duration $T = 51\ \mu\text{s}$ is sampled in 256 points and the frequency slope $K = 70.295\ \text{MHz}/\mu\text{s}$. Unless otherwise noted, the MIMO arrays are calibrated before the image reconstruction process as detailed in Section VI, and the images are reconstructed by the RMA for MIMO-SAR as proposed in Section VII-B.

A. POINT SPREAD FUNCTION

In order to validate the experimental setups and to demonstrate different performance metrics (i.e., image resolution, calibration, etc.), the point spread function (PSF) is firstly measured using a corner reflector placed at a distance of $z_0 = 800$ mm in front of the scanner. In these measurements, the imaging testbed version I, which is detailed in Section III-A, is used. The scanner, which moves the radar along both x and y axes, is configured such that a sampling distance of $\Delta_x \approx 1$ mm ($\approx \lambda/4$) and $\Delta_y \approx 7.59$ mm ($\approx 2\lambda$) is realized.

First, the effect of aperture size on the PSF is shown in Fig. 16. The results in Fig. 16a and Fig. 16b demonstrate the measured PSFs along the y -axis when the SAR aperture lengths are $D_y^S \approx 200$ mm and $D_y^S \approx 400$ mm, respectively. As given in [44], [56], the theoretical image resolution is about $\delta_x = \delta_y \approx 7.6$ mm in both axes when the aperture size is 200 mm by 200 mm. The resolution is improved to $\delta_x = \delta_y \approx 3.8$ mm when the aperture size becomes 400 mm by 400 mm. In Fig. 16, the measured PSFs are also validated using the simulated versions. As shown in both Fig. 16a and Fig. 16b, the measured PSFs demonstrate the same theoretical counterpart in different scenarios.

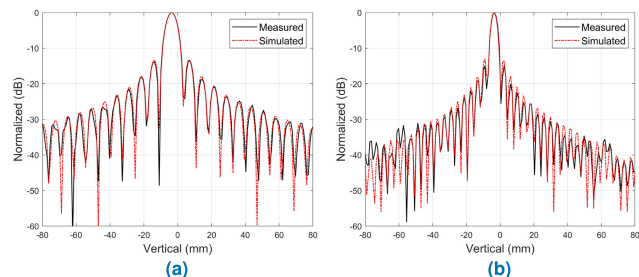


FIGURE 16. The measured and simulated point spread functions along the y -axis created using a corner reflector located at $z_0 \approx 800$ mm, where (a) $D_y^S \approx 200$ mm, and (b) $D_y^S \approx 400$ mm.

To demonstrate the performance of the presented algorithms with real data, we measure the PSF using a corner reflector placed at a distance of $z_0 = 400$ mm in front of the

scanner. In this measurement, the imaging testbed version III, which is detailed in Section III-C, is used. The scanner moves the radar along the x -axis to capture data at $N_x = 101$ horizontal points with a sampling distance of $\Delta_x \approx 1$ mm. The data in this experiment is captured at a single vertical point (i.e., $N_y = 1$). Therefore, a SAR aperture size of $D_x^S \approx 100$ mm by $D_y^S \approx 82.88$ mm ($\approx 85\lambda/4$) is created.

The image shown in Fig. 17a is reconstructed using the RMA for MIMO-SAR presented in Section VII-B, where the multistatic-to-monostatic conversion operation is applied based on off-center of the target in z axis ((x_0, y_0, z_0) = (0, 0, 700 mm)). The image shown in Fig. 17b is reconstructed using the RMA for MIMO-SAR after implementing the multistatic-to-monostatic conversion according to the center of the target ((x_0, y_0, z_0) = (0, 0, 400 mm)). Comparing both images, we can see that the image is distorted as the target pixel departs from the selected reference point.

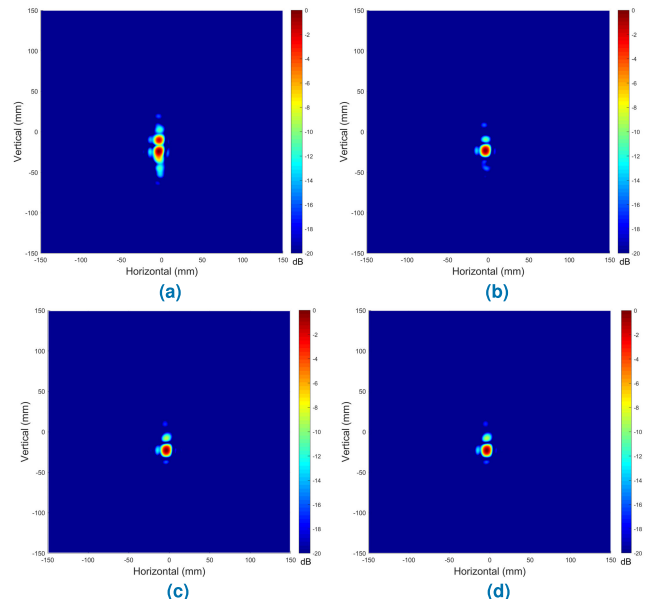


FIGURE 17. Comparison of the measured point spread functions created using different imaging algorithms. Reconstructed images using: (a) the RMA for MIMO-SAR after the multistatic-to-monostatic conversion based on off-center of the target in z -axis, (b) the RMA for MIMO-SAR with the conversion based on the center of the target, (c) the SIMO-SAR based algorithm, and (d) the enhanced BPA.

In Fig. 17c and Fig. 17d, the images reconstructed using the SIMO-SAR based approach proposed in Section VII-C and the enhanced BPA detailed in Section VII-A are depicted, respectively. It can be concluded that the results obtained by the SIMO-SAR based algorithm and the enhanced BPA are of high consistency at 20 dB dynamic range. Besides, for the antenna layout of the four-chip cascaded board, the RMA for MIMO-SAR can achieve a similar imaging performance with the enhanced BPA and SIMO-SAR based reconstruction as long as the multistatic-to-monostatic conversion operation is applied according to an appropriate reference point.

Finally, the importance of the multi-channel MIMO array calibration in high-resolution imaging is demonstrated

in Fig. 18 using the imaging testbed version II, which is detailed in Section III-B. Fig. 18a and Fig. 18b compare the PSFs along the y -axis created using both calibrated and non-calibrated measured data when the SAR aperture sizes are $D_y^S \approx 200$ mm and $D_y^S \approx 400$ mm, respectively. In both figures, it is shown that the proposed calibration method suppresses the grating lobes caused by the phase mismatches between the MIMO channels for more than 20 dB.

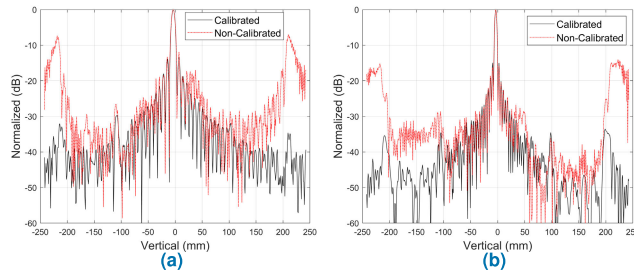


FIGURE 18. The effect of calibration on the measured point spread function along the y -axis (target is located at $z_0 \approx 800$ mm), where (a) $D_y^S \approx 200$ mm, and (b) $D_y^S \approx 400$ mm.

B. IMAGING RESULTS WITH SINGLE-CHIP SENSORS

To demonstrate the effectiveness of the testbed version II in 3-D holographic imaging, a test target with dimensions 100 mm by 150 mm (shown in Fig. 19a) cut out from a copper-clad laminate is used. In this scenario, the target is placed at a distance of $z_0 \approx 285$ mm from the scanner. The SAR aperture is synthesized to cover an area of $D_x^S \approx 400$ by $D_y^S \approx 400$ mm. The reconstructed 3-D volumetric image, which is visualized using the MATLAB volume viewer [65] application, is shown in Fig. 19b. Fig. 19c, which depicts the same 3-D image projected in 2-D space using maximum intensity projection (MIP) technique, identifies the target with no artifacts at 20 dB dynamic range. Fig. 19d illustrates the impact of the testbed synchronization in MIMO-SAR imaging. In this result, the novel radar-scanner synchronization approach developed in Section IV is not used, and a synchronization error of up to ± 5 samples per horizontal scanning is injected during the data capture. It is clearly visible that the synchronization step is very critical at the testbed development process to achieve a higher quality of images.

The imaging scenario in Fig. 20a shows multiple objects (two different wire cutters, a pair of scissors, a wire stripper, and a pair of tweezers) concealed in a cardboard box. In this experiment, the imaging testbed version I is used, and a SAR aperture size of 400 mm \times 400 mm is created. The spatial sampling intervals are selected as $\Delta_x \approx 0.98$ mm and $\Delta_y = 7.59$ mm. Fig. 20b shows the reconstructed 3-D volumetric image, where all the objects are clearly visible. In this experimental result, the ImageJ [82] application is utilized to visualize the reconstructed 3-D holographic image. The reconstructed 2-D image slice version of this image is given in [56].

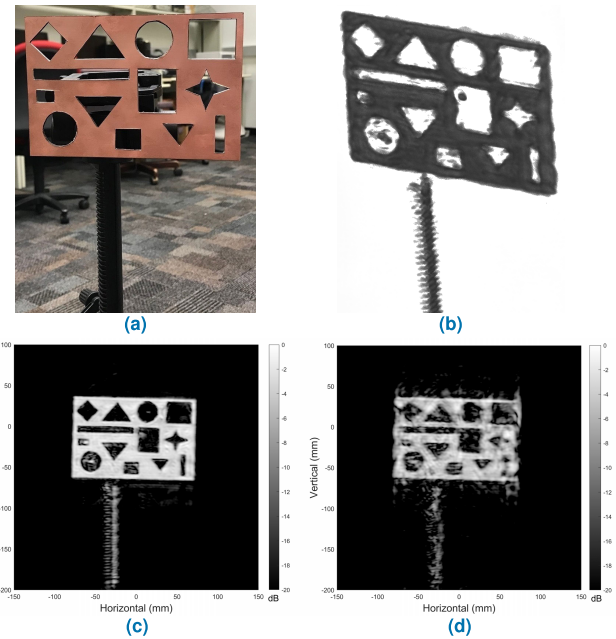


FIGURE 19. Imaging scenario with a test target: (a) optical image, (b) reconstructed image in 3-D volumetric view, (c) reconstructed 3-D image projected in 2-D space using MIP technique, and (d) reconstructed 3-D image in 2-D MIP view when there is a synchronization error of up to ± 5 samples per horizontal scanning.

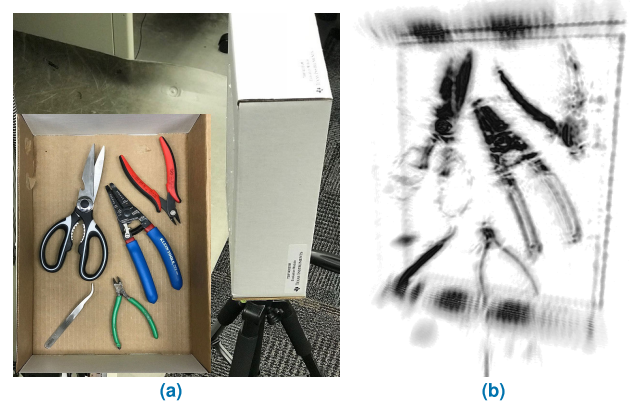


FIGURE 20. Imaging scenario with multiple objects concealed in a cardboard box: (a) optical image, and (b) reconstructed image in 3-D volumetric view.

3-D printing technology has gained popularity nowadays as it contributes to a wide range of applications. As a result of the high dependency on this technology, NDT techniques are required by the industry [83]. Here, we perform an experiment using the imaging testbed version I for the purpose of the NDT of a 3-D plastic object printed using polylactic acid (PLA) material as shown in Fig. 21a. In this scenario, the target is placed at a mean distance of $z_0 \approx 210$ mm from the scanner. The SAR aperture is synthesized to cover an area of $D_x^S \approx 400$ mm by $D_y^S \approx 400$ mm. Fig. 21b shows the reconstructed 3-D image projected in 2-D space using MIP technique. According to visual inspection of the obtained result, the shape of the 3-D printed plastic object can

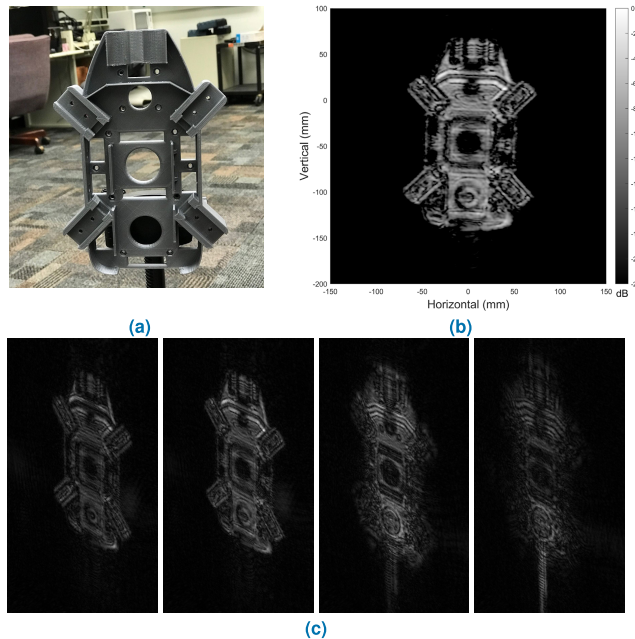


FIGURE 21. Imaging scenario with a plastic item: (a) optical image, (b) reconstructed 3-D image projected in 2-D space using MIP technique, and (c) reconstructed 2-D image slices along the z -axis (z is increasing from left to right).

be clearly noticed. The reconstructed 2-D image slices along the z -axis are depicted in Fig. 21c to show the reconstruction performance in the range domain.

With the rise of concern about public security, automatically detecting the potential threats and dangerous objects concealed under clothes or hidden inside bags becomes an urgent issue in the security check systems. Hence, to demonstrate a similar concealed item scenario, we use a target scene consists of a mannequin dressed with a coat and a knife under its cloth. A knife composed of a stainless steel blade and a plastic handle is concealed under the mannequin's jacket and located at a mean distance of $z_0 \approx 1000$ mm from the scanner as shown in Fig. 22a. In this experiment, the imaging testbed version II is used. The SAR aperture is synthesized to cover an area of $D_x^S \approx 512$ mm by $D_y^S \approx 720$ mm.

Fig. 22b is the projected view (using the MIP technique) of the 3-D image result onto the xy plane. It can be seen that the radiated waves pass through the clothing material and are reflected by the body and the concealed knife. The shapes and the intensity of the targets, such as the knife handle, blade, and the mannequin, are clearly apparent in the reconstructed image.

A final experiment is performed to demonstrate the capability of the prototyped solution in through-wall imaging applications. Fig. 23 shows the imaging scenario consists of a metal strip with a size of 10 mm by 5 mm by 450 mm concealed behind a drywall. The thickness of the drywall is 20 mm, and its size is 600 mm by 500 mm as shown in Fig. 23a. As depicted in Fig. 23b, the metal strip attached to a plastic tripod is located at a distance of 1000 mm in

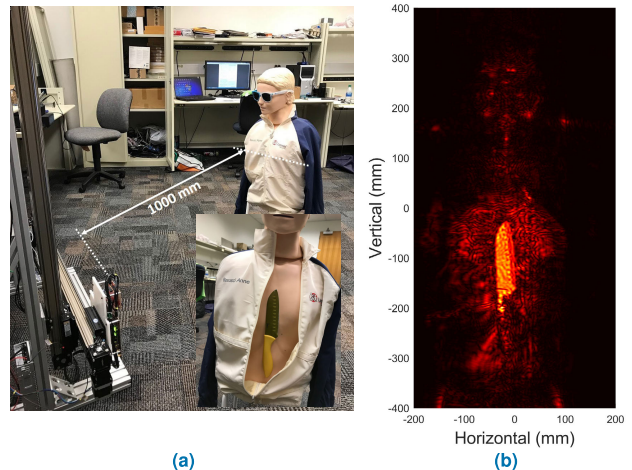


FIGURE 22. (a) Photograph of the human body model carrying a concealed knife located at a distance of 1000 mm. (b) Reconstructed 3-D image projected in 2-D space using MIP technique.

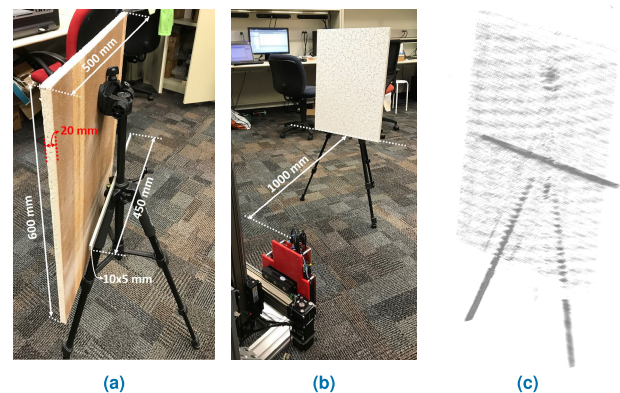


FIGURE 23. (a) Photograph of the small metal strip concealed behind a drywall and (b) located at a distance of 1000 mm. (c) Reconstructed image in 3-D volumetric view.

front of the scanner. In this experiment, the imaging testbed version II is used. Fig. 23c shows the reconstructed 3-D volumetric image. The metal strip is clearly identified, and the non-metallic tripod is visible.

C. IMAGING RESULTS WITH MULTI-CHIP CASCADED SENSORS

In this section, to verify the effectiveness of the imaging testbed version III and to demonstrate the performance metrics of the proposed signal processing steps, experimental image results of a concealed item scenario are provided. In this scenario, a pair of scissors concealed in a cardboard box is placed at a mean distance of $z_0 \approx 250$ mm from the scanner as shown in Fig. 24. The spatial sampling intervals are selected as $\Delta_x = \lambda/4 \approx 1$ mm and $\Delta_y = 86\lambda/4 \approx 83$ mm along x and y axes, respectively. The SAR aperture is synthesized to cover an area of $D_x^S \approx 500$ mm ($N_x = 500$) by $D_y^S \approx 500$ mm ($N_y = 6$).

Fig. 25a and Fig. 25b show the imaging results of the RMA for MIMO-SAR without the multistatic-to-monostatic conversion operation and after implementing the conversion

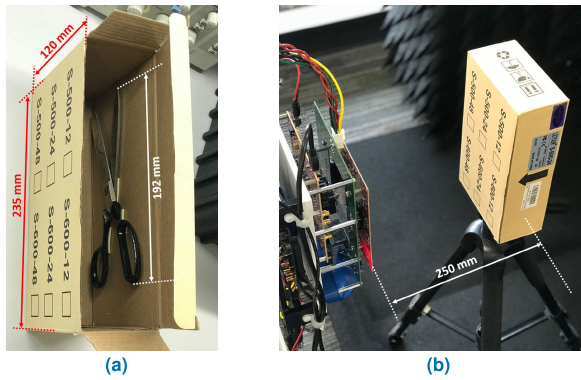


FIGURE 24. Imaging scenario with the scissors (a) concealed in a cardboard box and (b) located at a mean distance of $z_0 \approx 250$ mm from the scanner.

based on off-center of the target in xy axis ($x_0 = y_0 = -50$ mm), respectively. In Fig. 25c, the RMA image is reconstructed after implementing the multistatic-to-monostatic conversion based on the center of the target ((x_0, y_0, z_0) = (0, 0, 250 mm)).

Comparing the first three results, it can be concluded that the RMA can not be directly applied to the multistatic data in short-range imaging. The RMA result in Fig. 25a based on the monostatic assumption shows obvious defocusing in the image, which indicates that the typical virtual channel approximations are no longer suitable for short-range MIMO-SAR imaging. It is clearly visible in Fig. 25b that the image distortion in RMA caused by the multistatic-to-monostatic conversion increases as the target pixels depart from the reference point. Hence, only the image in Fig. 25c, where the multistatic data is compensated based on a reference point close to the center of the target, provides a truthful reconstruction of the target at 20 dB dynamic range.

Fig. 25d and Fig. 25e show the images of the same target reconstructed using the SIMO-SAR based algorithm (as detailed in Section VII-C). In Fig. 25d, the MIMO array calibration method proposed in Section VI is not applied to the sensor data before the image reconstruction. In this result, it is presented that the calibration process is very critical for the quality of images. Fig. 25e shows the image reconstruction performance of the SIMO-SAR based algorithm after implementing the proposed MIMO array calibration approach. Therefore, the effectiveness of the proposed calibration approach in MIMO-SAR imaging is depicted. Finally, Fig. 25f shows the image of the same target reconstructed with the calibrated data using the enhanced BPA (as detailed in Section VII-A).

Comparing both Fig. 25c and Fig. 25e, the improvement in image quality of the SIMO-SAR based reconstruction (compared with the RMA for MIMO-SAR) becomes visible when the target size increases (i.e., the target pixels depart from the reference point), but the trade-off is the increased computational complexity as discussed in Section VII. Besides, comparing both Fig. 25e and Fig. 25f, we can see that the results obtained by the SIMO-SAR based algorithm

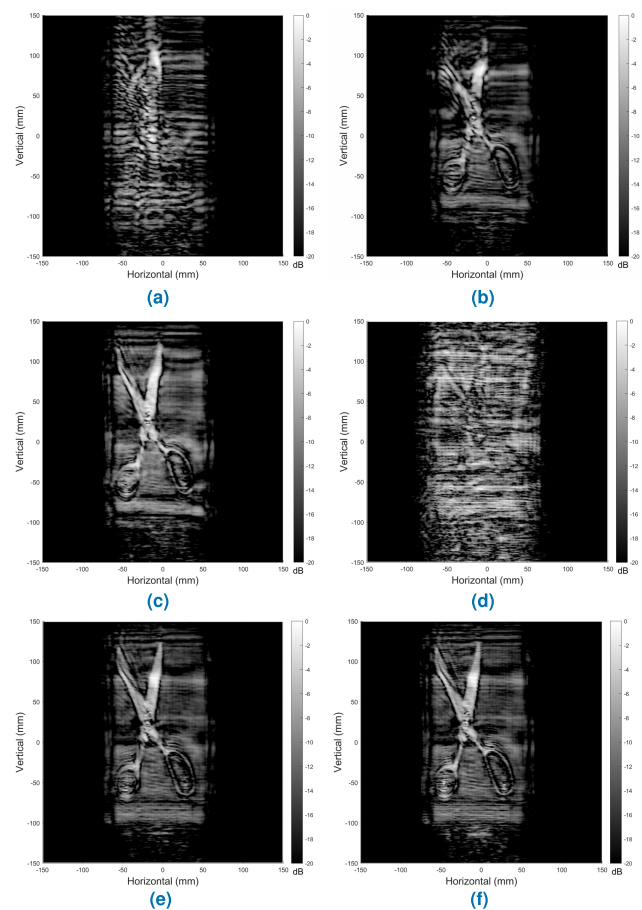


FIGURE 25. Imaging results (in 2-D MIP view) of the experimental scenario with a concealed pair of scissors. Reconstructed images using the RMA for MIMO-SAR: (a) without the multistatic-to-monostatic conversion, (b) with the conversion based on off-center of the target in xy -axes, and (c) with the conversion based on the center of the target. Reconstructed images using the SIMO-SAR based algorithm: (d) without the MIMO array calibration, (e) with the calibrated MIMO data, (f) Reconstructed image using the enhanced BPA.

and the enhanced BPA are of high consistency. The target image is well resolved in both images without any artifact in the 20 dB dynamic range, which verifies the effectiveness of both algorithms in MIMO-SAR image reconstruction.

IX. CONCLUSIONS

In this paper, we designed, implemented, and experimentally validated different types of system-level MIMO-SAR imaging testbeds utilizing commercially available MIMO mmWave sensors in SAR configuration. We first developed a version I testbed with limited speed and aperture size to demonstrate the proof-of-concept. We then improved the testbed in version II with a much faster and bigger mechanical scanner along with a novel synchronization approach between the radar sensors and the scanners. We finally integrated the state-of-the-art multi-chip cascaded mmWave sensors with larger MIMO apertures in version III to reduce the total scanning time. We investigated the overall hardware architecture of each system in detail. To control the entire signal processing chain from data capture

to image reconstruction, an open-source MATLAB-based toolbox was introduced. Furthermore, to compensate for the gain and phase mismatches in the MIMO array, a practical multi-channel array calibration method, which is an important signal processing step in 3-D MIMO-SAR imaging, was proposed. We reviewed and experimentally verified image reconstruction algorithms for MIMO-SAR configurations in short-range applications. More importantly, we provided real imaging results obtained using the prototyped MIMO-SAR testbeds to demonstrate the effectiveness of the proposed solution in high-resolution 3-D holographic imaging applications.

REFERENCES

- [1] L. Chao, M. N. Afsar, and K. A. Korolev, "Millimeter wave dielectric spectroscopy and breast cancer imaging," in *Proc. 7th Eur. Microw. Integr. Circuit Conf.*, Amsterdam, The Netherlands, Oct. 2012, pp. 572–575.
- [2] S. Di Meo, G. Matrone, M. Pasian, M. Bozzi, L. Perregini, G. Magenes, A. Mazzanti, F. Svelto, P. E. Summers, G. Renne, L. Preda, and M. Bellomi, "High-resolution mm-wave imaging techniques and systems for breast cancer detection," in *IEEE MTT-S Int. Microw. Symp. Dig.*, Pavia, Italy, Sep. 2017, pp. 1–3.
- [3] Y. Gao and R. Zoughi, "Millimeter wave reflectometry and imaging for noninvasive diagnosis of skin burn injuries," *IEEE Trans. Instrum. Meas.*, vol. 66, no. 1, pp. 77–84, Jan. 2017.
- [4] A. Mirbeik-Sabzevari, S. Li, E. Garay, H.-T. Nguyen, H. Wang, and N. Tavassolian, "Synthetic ultra-high-resolution millimeter-wave imaging for skin cancer detection," *IEEE Trans. Biomed. Eng.*, vol. 66, no. 1, pp. 61–71, Jan. 2019.
- [5] A. Mirbeik-Sabzevari, N. Tavassolian, and R. Ashinoff, "Ultra-high-resolution millimeter-wave imaging: A new promising skin cancer imaging modality," in *Proc. IEEE Biomed. Circuits Syst. Conf. (BioCAS)*, Cleveland, OH, USA, Oct. 2018, pp. 1–4.
- [6] D. M. Sheen, D. L. McMakin, and T. E. Hall, "Three-dimensional millimeter-wave imaging for concealed weapon detection," *IEEE Trans. Microw. Theory Techn.*, vol. 49, no. 9, pp. 1581–1592, Sep. 2001.
- [7] X. Zhuge and A. G. Yarovoy, "A sparse aperture MIMO-SAR-based UWB imaging system for concealed weapon detection," *IEEE Trans. Geosci. Remote Sens.*, vol. 49, no. 1, pp. 509–518, Jan. 2011.
- [8] S. Ahmed, A. Schiessl, F. Gumbmann, M. Tiebout, S. Methfessel, and L.-P. Schmidt, "Advanced microwave imaging," *IEEE Microw. Mag.*, vol. 13, no. 6, pp. 26–43, Sep. 2012.
- [9] R. Appleby and R. N. Anderton, "Millimeter-wave and submillimeter-wave imaging for security and surveillance," *Proc. IEEE*, vol. 95, no. 8, pp. 1683–1690, Aug. 2007.
- [10] J. L. Fernandes, J. R. Tedeschi, D. M. Sheen, and D. L. McMakin, "Three-dimensional millimeter-wave imaging for concealed threat detection in shoes," *Proc. SPIE*, vol. 8715, pp. C1–C8, May 2013.
- [11] M. E. Yanik and M. Torlak, "Near-field 2-D SAR imaging by millimeter-wave radar for concealed item detection," in *Proc. IEEE Radio Wireless Symp. (RWS)*, Orlando, FL, USA, Jan. 2019, pp. 1–4.
- [12] T. Liu, Y. Zhao, Y. Wei, Y. Zhao, and S. Wei, "Concealed object detection for activate millimeter wave image," *IEEE Trans. Ind. Electron.*, vol. 66, no. 12, pp. 9909–9917, Dec. 2019.
- [13] D. M. Sheen, H. D. Collins, T. E. Hall, D. L. McMakin, R. P. Gribble, R. H. Severtsen, J. M. Prince, and L. D. Reid, "Real-time wideband holographic surveillance system," U.S. Patent 5 557 283 A, Sep. 17, 1996.
- [14] S. Kharkovsky, J. T. Case, M. A. Abou-Khousa, R. Zoughi, and F. L. Hepburn, "Millimeter-wave detection of localized anomalies in the space shuttle external fuel tank insulating foam," *IEEE Trans. Instrum. Meas.*, vol. 55, no. 4, pp. 1250–1257, Aug. 2006.
- [15] S. Kharkovsky and R. Zoughi, "Microwave and millimeter wave non-destructive testing and evaluation—overview and recent advances," *IEEE Instrum. Meas. Mag.*, vol. 10, no. 2, pp. 26–38, Apr. 2007.
- [16] M. T. Ghasr, S. Kharkovsky, R. Bohnert, B. Hirst, and R. Zoughi, "30 GHz linear high-resolution and rapid millimeter wave imaging system for NDE," *IEEE Trans. Antennas Propag.*, vol. 61, no. 9, pp. 4733–4740, Sep. 2013.
- [17] C. J. Li and H. Ling, "High-resolution, downward-looking radar imaging using a small consumer drone," in *Proc. IEEE Int. Symp. Antennas Propag. (APSURSI)*, Fajardo, Puerto Rico, Jun. 2016, pp. 2037–2038.
- [18] D. S. Goshi, C. Rhoads, J. McKitterick, and T. Case, "Millimeter wave imaging for fixed wing zero visibility landing," *Proc. SPIE*, vol. 10994, pp. 29–42, May 2019.
- [19] G. Rankin, A. Tirkel, and A. Leukhin, "Millimeter wave array for UAV imaging MIMO radar," in *Proc. 16th Int. Radar Symp. (IRS)*, Dresden, Germany, Jun. 2015, pp. 499–504.
- [20] G. Y. Tian, A. Al-Qubaa, and J. Wilson, "Design of an electromagnetic imaging system for weapon detection based on GMR sensor arrays," *Sens. Actuators A, Phys.*, vol. 174, pp. 75–84, Feb. 2012.
- [21] S. S. Ahmed, A. Genghamer, A. Schiessl, and L.-P. Schmidt, "Fully electronic E-band personnel imager of 2 m² aperture based on a multi-static architecture," *IEEE Trans. Microw. Theory Techn.*, vol. 61, no. 1, pp. 651–657, Jan. 2013.
- [22] K. Ramasubramanian and J. Singh, "AWR1443 single-chip radar: For diverse proximity-sensing applications," Texas Instrum., Dallas, TX, USA, Tech. Rep. SPYY008, May 2017.
- [23] D. W. Bliss and K. W. Forsythe, "Multiple-input multiple-output (MIMO) radar and imaging: Degrees of freedom and resolution," in *Proc. 37th Asilomar Conf. Signals, Syst. Comput.*, Pacific Grove, CA, USA, vol. 1, Nov. 2003, pp. 54–59.
- [24] J. Li and P. Stoica, *MIMO Radar Signal Processing*. Hoboken, NJ, USA: Wiley, 2009.
- [25] J. Li and P. Stoica, "MIMO radar with colocated antennas," *IEEE Signal Process. Mag.*, vol. 24, no. 5, pp. 106–114, Sep. 2007.
- [26] M. A. Richards, "A beginner's guide to interferometric SAR concepts and signal processing [AESS tutorial IV]," *IEEE Aerosp. Electron. Syst. Mag.*, vol. 22, no. 9, pp. 5–29, Sep. 2007.
- [27] G. Franceschetti and R. Lanari, *Synthetic Aperture Radar Processing*. New York, NY, USA: CRC Press, 1999.
- [28] T. Savelyev, X. Zhuge, B. Yang, P. Aubry, A. Yarovoy, L. Lighthart, and B. Levitas, "Comparison of 10–18 GHz SAR and MIMO-based short-range imaging radars," *Int. J. Microw. Wireless Technol.*, vol. 2, nos. 3–4, pp. 369–377, Aug. 2010.
- [29] D. Sheen, D. McMakin, and T. Hall, "Near-field three-dimensional radar imaging techniques and applications," *Appl. Opt.*, vol. 49, no. 19, pp. E83–E93, Jul. 2010.
- [30] N. Mohammadian, O. Furxhi, R. E. Short, and R. Driggers, "SAR millimeter wave imaging systems," *Proc. SPIE*, vol. 10994, pp. 86–98, May 2019.
- [31] J. Gao, Y. Qin, B. Deng, H. Wang, and X. Li, "Novel efficient 3D short-range imaging algorithms for a scanning 1D-MIMO array," *IEEE Trans. Image Process.*, vol. 27, no. 7, pp. 3631–3643, Jul. 2018.
- [32] B. Fan, J.-K. Gao, H.-J. Li, Z.-J. Jiang, and Y. He, "Near-field 3D SAR imaging using a scanning linear MIMO array with arbitrary topologies," *IEEE Access*, vol. 8, pp. 6782–6791, Dec. 2020.
- [33] J. Gao, B. Deng, Y. Qin, H. Wang, and X. Li, "An efficient algorithm for MIMO cylindrical millimeter-wave holographic 3-D imaging," *IEEE Trans. Microw. Theory Techn.*, vol. 66, no. 11, pp. 5065–5074, Nov. 2018.
- [34] An Open-Source MATLAB-Based MIMO-SAR mmWave Imaging Toolbox. Accessed: Jun. 2020. [Online]. Available: <https://github.com/meminyanik/MIMO-SAR-mmWave-Imaging-Toolbox>
- [35] H. Gao, C. Li, S. Wu, H. Geng, S. Zheng, X. Qu, and G. Fang, "Study of the extended phase shift migration for three-dimensional MIMO-SAR imaging in terahertz band," *IEEE Access*, vol. 8, pp. 24773–24783, Jan. 2020.
- [36] M. Soumekh, "Wide-bandwidth continuous-wave monostatic/bistatic synthetic aperture radar imaging," in *Proc. Int. Conf. Image Process. (ICIP)*, Chicago, IL, USA, vol. 3, Oct. 1998, pp. 361–365.
- [37] J. Moll, P. Schops, and V. Krozer, "Towards three-dimensional millimeter-wave radar with the bistatic fast-factorized back-projection algorithm—potential and limitations," *IEEE Trans. THz Sci. Technol.*, vol. 2, no. 4, pp. 432–440, Jul. 2012.
- [38] M. Abbasi, A. Shayei, M. Shabany, and Z. Kavehvash, "Fast Fourier-based implementation of synthetic aperture radar algorithm for multistatic imaging system," *IEEE Trans. Instrum. Meas.*, vol. 68, no. 9, pp. 3339–3349, Sep. 2019.
- [39] J. M. Lopez-Sahcznez and J. Fortuny-Guasch, "3-D radar imaging using range migration techniques," *IEEE Trans. Antennas Propag.*, vol. 48, no. 5, pp. 728–737, May 2000.
- [40] J. Fortuny-Guasch and J. N. Lopez-Sanchez, "Extension of the 3-D range migration algorithm to cylindrical and spherical scanning geometries," *IEEE Trans. Antennas Propag.*, vol. 49, no. 10, pp. 1434–1444, Oct. 2001.

- [41] W. F. Moulder, J. D. Krieger, J. J. Majewski, C. M. Coldwell, H. T. Nguyen, D. T. Maurais-Galejs, T. L. Anderson, P. Dufilie, and J. S. Herd, "Development of a high-throughput microwave imaging system for concealed weapons detection," in *Proc. IEEE Int. Symp. Phased Array Syst. Technol. (PAST)*, Waltham, MA, USA, Oct. 2016, pp. 1–6.
- [42] Z. Wang, Q. Guo, X. Tian, T. Chang, and H.-L. Cui, "Near-field 3-D millimeter-wave imaging using MIMO RMA with range compensation," *IEEE Trans. Microw. Theory Techn.*, vol. 67, no. 3, pp. 1157–1166, Mar. 2019.
- [43] R. Zhu, J. Zhou, L. Tang, Y. Kan, and Q. Fu, "Frequency-domain imaging algorithm for single-input–multiple-output array," *IEEE Geosci. Remote Sens. Lett.*, vol. 13, no. 12, pp. 1747–1751, Dec. 2016.
- [44] X. Zhuge and A. G. Yarovoy, "Three-dimensional near-field MIMO array imaging using range migration techniques," *IEEE Trans. Image Process.*, vol. 21, no. 6, pp. 3026–3033, Jun. 2012.
- [45] L. Qiao, Y. Wang, Z. Zhao, and Z. Chen, "Exact reconstruction for near-field three-dimensional planar millimeter-wave holographic imaging," *J. Infr., Millim., THz Waves*, vol. 36, no. 12, pp. 1221–1236, Dec. 2015.
- [46] A. Meta, P. Hoogeboom, and L. P. Ligthart, "Signal processing for FMCW SAR," *IEEE Trans. Geosci. Remote Sens.*, vol. 45, no. 11, pp. 3519–3532, Nov. 2007.
- [47] G. Wang, J.-M. Munoz-Ferreras, C. Gu, C. Li, and R. Gomez-Garcia, "Application of linear-frequency-modulated continuous-wave (LFMCW) radars for tracking of vital signs," *IEEE Trans. Microw. Theory Techn.*, vol. 62, no. 6, pp. 1387–1399, Jun. 2014.
- [48] L. Ding, M. Ali, S. Patole, and A. Dabak, "Vibration parameter estimation using FMCW radar," in *Proc. IEEE Int. Conf. Acoust., Speech Signal Process. (ICASSP)*, Shanghai, China, Mar. 2016, pp. 2224–2228.
- [49] R. Zhu, J. Zhou, G. Jiang, and Q. Fu, "Range migration algorithm for near-field MIMO-SAR imaging," *IEEE Geosci. Remote Sens. Lett.*, vol. 14, no. 12, pp. 2280–2284, Dec. 2017.
- [50] R. Zhu, J. Zhou, L. Zhao, and Q. Fu, "Frequency-domain algorithm for short-range MIMO-SAR imaging," in *Proc. Int. Conf. Radar Syst. (Radar)*, Belfast, U.K., Oct. 2017, pp. 1–4.
- [51] R. Zhu, J. Zhou, B. Cheng, Q. Fu, and G. Jiang, "Sequential frequency-domain imaging algorithm for near-field MIMO-SAR with arbitrary scanning paths," *IEEE J. Sel. Topics Appl. Earth Observ. Remote Sens.*, vol. 12, no. 8, pp. 2967–2975, Aug. 2019.
- [52] G. Krieger, "MIMO-SAR: Opportunities and pitfalls," *IEEE Trans. Geosci. Remote Sens.*, vol. 52, no. 5, pp. 2628–2645, May 2014.
- [53] Texas Instruments. *The Overview of the TI's mmWave Sensors*. Accessed: Jun. 2020. [Online]. Available: <http://www.ti.com/sensors/mmwave/overview.html>
- [54] Texas Instruments. *Building Cascade Radar Using TI's mmWave Sensors*. Accessed: Jun. 2020. [Online]. Available: <https://training.ti.com/build-cascaded-radar-using-tis-mmwave-sensors>
- [55] *Imaging Radar Using Cascaded mmWave Sensor Reference Design*. Accessed: Jun. 2020. [Online]. Available: <http://www.ti.com/tool/TIDEP-01012>
- [56] M. E. Yanik and M. Torlak, "Near-field MIMO-SAR millimeter-wave imaging with sparsely sampled aperture data," *IEEE Access*, vol. 7, pp. 31801–31819, 2019.
- [57] J. H. G. Ender and J. Klare, "System architectures and algorithms for radar imaging by MIMO-SAR," in *Proc. IEEE Radar Conf.*, Pasadena, CA, USA, May 2009, pp. 1–6.
- [58] Y. Qi, Y. Wang, W. Tan, and W. Hong, "Application of sparse array and MIMO in near-range microwave imaging," *Proc. SPIE*, vol. 8179, Oct. 2011, Art. no. 81790X.
- [59] M. E. Yanik and M. Torlak, "Millimeter-wave near-field imaging with two-dimensional SAR data," in *Proc. SRC Techcon*, Austin, TX, USA, Sep. 2018, pp. 1–5.
- [60] M. E. Yanik, D. Wang, and M. Torlak, "3-D MIMO-SAR imaging using multi-chip cascaded millimeter-wave sensors," in *Proc. IEEE Global Conf. Signal Inf. Process. (GlobalSIP)*, Ottawa, ON, Canada, Nov. 2019, pp. 1–5.
- [61] *The FUYU Series of Ball Screw and Belt-Driven Linear Rails and Motion Controllers*. Accessed: Jun. 2020. [Online]. Available: <https://www.fuyumotion.com>
- [62] *The MJUNIT Series of Belt-Driven Linear Rails*. Accessed: Jun. 2020. [Online]. Available: <http://www.mjunit.com>
- [63] *Espressif ESP32 System-On-Chip Microcontrollers*. Accessed: Jun. 2020. [Online]. Available: <https://www.espressif.com/en/products/hardware/esp32/overview>
- [64] *The Free RTOS Kernel*. Accessed: Jun. 2020. [Online]. Available: <https://www.freertos.org/>
- [65] *MATLAB and Simulink for Technical Computing*. Accessed: Jun. 2020. [Online]. Available: <http://www.mathworks.com>
- [66] B. Poh Ng, J. P. Lie, M. Hwa Er, and A. Feng, "A practical simple geometry and Gain/Phase calibration technique for antenna array processing," *IEEE Trans. Antennas Propag.*, vol. 57, no. 7, pp. 1963–1972, Jul. 2009.
- [67] C. M. Schmid, C. Pfeffer, R. Feger, and A. Stelzer, "An FMCW MIMO radar calibration and mutual coupling compensation approach," in *Proc. Eur. Radar Conf.*, Nuremberg, Germany, Oct. 2013, pp. 13–16.
- [68] H. M. Aumann, A. J. Fenn, and F. G. Willwerth, "Phased array antenna calibration and pattern prediction using mutual coupling measurements," *IEEE Trans. Antennas Propag.*, vol. 37, no. 7, pp. 844–850, Jul. 1989.
- [69] J. Guetlein, A. Kirschner, and J. Detlefsen, "Calibration strategy for a TDM FMCW MIMO radar system," in *Proc. IEEE Int. Conf. Microw., Commun., Antennas Electron. Syst. (COMCAS)*, Tel Aviv-Yafo, Israel, Oct. 2013, pp. 1–5.
- [70] X. Tian, Q. Guo, T. Chang, and H.-L. Cui, "Phase self-calibration for millimeter wave MIMO imaging," in *Proc. 43rd Int. Conf. Infr., Millim., THz Waves (IRMMW-THz)*, Nagoya, Japan, Sep. 2018, pp. 1–2.
- [71] J.-W. Ting, D. Oloumi, and K. Rambabu, "FMCW SAR system for near-distance imaging applications—practical considerations and calibrations," *IEEE Trans. Microw. Theory Techn.*, vol. 66, no. 1, pp. 450–461, Jan. 2018.
- [72] M. Z. Ikram, M. Ali, and D. Wang, "Joint antenna-array calibration and direction of arrival estimation for automotive radars," in *Proc. IEEE Radar Conf. (RadarConf)*, Philadelphia, PA, USA, May 2016, pp. 1–5.
- [73] H. Deng, G. Farquharson, J. Sahr, Y. Goncharenko, and J. Mower, "Phase calibration of an along-track interferometric FMCW SAR," *IEEE Trans. Geosci. Remote Sens.*, vol. 56, no. 8, pp. 4876–4886, Aug. 2018.
- [74] H. Singh, H. L. Sneha, and R. M. Jha, "Mutual coupling in phased arrays: A review," *Int. J. Antennas Propag.*, vol. 2013, pp. 1–23, Mar. 2013.
- [75] M. E. Yanik and M. Torlak, "Geolocalization via tracking of wideband radio astronomical sources in the presence of radio frequency interference," in *Proc. IEEE/ION Position, Location Navigat. Symp. (PLANS)*, Monterey, CA, USA, Apr. 2018, pp. 1234–1238.
- [76] D. Rife and R. Boorstyn, "Single tone parameter estimation from discrete-time observations," *IEEE Trans. Inf. Theory*, vol. 20, no. 5, pp. 591–598, Sep. 1974.
- [77] M. D. Buhari, G. Y. Tian, R. Tiwari, and A. H. Muqaibel, "Multicarrier SAR image reconstruction using integrated MUSIC-LSE algorithm," *IEEE Access*, vol. 6, pp. 22827–22838, 2018.
- [78] H. Weyl, "Ausbreitung elektromagnetischer wellen über einem ebenen leiter," *Annalen der Physik*, vol. 365, no. 21, pp. 481–500, 1919.
- [79] L. M. Brekhovskikh and O. A. Godin, *Acoustics of Layered Media II: Point Sources and Bounded Beams*. New York, NY, USA: Springer, 1999.
- [80] R. H. Stolt, "Migration by Fourier transform," *Geophysics*, vol. 43, no. 1, pp. 23–48, Feb. 1978.
- [81] V. Dham, "Programming chirp parameters in Texas Instrument radar devices," Texas Instrum., Dallas, TX, USA, Tech. Rep. SWRA553, May 2017.
- [82] *ImageJ: An Open Source Image Processing Program Designed for Scientific Multidimensional Images*. Accessed: Jun. 2020. [Online]. Available: <https://imagej.net/>
- [83] M. EL Saadouny, J. Barowski, J. Jebramcik, and I. Rolfs, "Millimeter wave SAR imaging for the non-destructive testing of 3D-printed samples," in *Proc. Int. Conf. Electromagn. Adv. Appl. (ICEAA)*, Granada, Spain, Sep. 2019, pp. 1283–1285.



MUHAMMET EMIN YANIK (Member, IEEE) received the B.S. and M.S. degrees in electrical and electronics engineering from Hacettepe University, in 2007 and 2010, respectively, and the Ph.D. degree in electrical engineering from The University of Texas at Dallas, in 2020. He joined Texas Instruments, in 2020, where he is currently a Systems Engineer, developing signal processing algorithms for mmWave radars. He was with Aselsan, Ankara, Turkey, from 2007 to 2016, where he has worked on real-time embedded system development for safety-critical avionics applications. In spring 2019, he has worked at Texas Instruments, where he developed novel 3-D holographic MIMO-SAR mmWave imaging algorithms and testbeds. He spent the summer of 2019 at Microsoft, developing software for the next-generation HoloLens mixed-reality smart glass. His current research interests include mmWave radars, ultrawideband radar imaging systems, and real-time embedded system development. He was a recipient of the Tubitak Graduate Fellowship, from 2007 to 2009, and the Turkcell Academy Fellowship, from 2012 to 2013.



DAN WANG (Senior Member, IEEE) received the M.S. degree in electrical engineering from the University of Minnesota–Twin Cities, in 2009, and the Ph.D. degree in electrical engineering from The University of Austin, in 2012. She joined Texas Instruments, in 2012, where she is currently a System Manager for developing radar system and algorithms for automotive and industry applications.



MURAT TORLAK (Senior Member, IEEE) received the M.S. and Ph.D. degrees in electrical engineering from The University of Texas at Austin, in 1995 and 1999, respectively. Since August 1999, he has been with the Department of Electrical Engineering, The University of Texas, where he has been promoted to the rank of a Full Professor. He spent the summers of 1997 and 1998 with Cwill Telecommunications, Inc., Austin, TX, USA, where he participated in the design of a smart antenna wireless local loop systems and directed research and development efforts towards standardization of TD-SCDMA for the International Telecommunication Union. He was a Visiting Scholar with the University of California at Berkeley, in 2008. He has been an Active Contributor in the areas of smart antennas and multiuser detection. His current research interests include millimeter-wave automotive radars, millimeter-wave imaging systems, cognitive radios, and interference mitigation in radio telescopes. He was the Program Chair of the IEEE Signal Processing Society Dallas Chapter, from 2003 to 2005. He has served on the Technical Program Committees (TPC) of the several IEEE conferences. He was the General Chair of Symposium on Millimeter Wave Imaging and Communications in 2013 IEEE GlobalSIP Conference. He has served as an Associate Editor for the IEEE TRANSACTIONS ON WIRELESS COMMUNICATIONS, from 2008 to 2013.

• • •